University of Illinois at Urbana-Champaign

ACRC

Air Conditioning and Refrigeration Center A National Science Foundation/University Cooperative Research Center

Experimental, Analytical and Finite Element Studies of the Nanoindentation Technique to Investigate Material Properties of Surface Layers Less Than 100 Nanometers Thick

N. Yu, A. A. Polycarpou, and T. F. Conry

ACRC TR-210 March 2003

For additional information:

Air Conditioning and Refrigeration Center
University of Illinois
Mechanical & Industrial Engineering Dept.
1206 West Green Street
Urbana, IL 61801

(217) 333-3115

Prepared as part of ACRC Project #127
Fundamental Investigation on the Tribological Failure Mechanisms of Compressor Surfaces -Scuffing
A. A. Polycarpou and T. F. Conry, Principal Investigators

The Air Conditioning and Refrigeration Center was founded in 1988 with a grant from the estate of Richard W. Kritzer, the founder of Peerless of America Inc. A State of Illinois Technology Challenge Grant helped build the laboratory facilities. The ACRC receives continuing support from the Richard W. Kritzer Endowment and the National Science Foundation. The following organizations have also become sponsors of the Center.

Alcan Aluminum Corporation
Amana Refrigeration, Inc.
Arçelik A. S.
Brazeway, Inc.
Carrier Corporation
Copeland Corporation
Dacor
Daikin Industries, Ltd.
Delphi Harrison Thermal Systems
Embraco S. A.
General Motors Corporation
Hill PHOENIX
Honeywell, Inc.
Hydro Aluminum Adrian, Inc.
Ingersoll-Rand Company
Kelon Electrical Holdings Co., Ltd.
Lennox International, Inc.
LG Electronics, Inc.
Modine Manufacturing Co.
Parker Hannifin Corporation
Peerless of America, Inc.
Samsung Electronics Co., Ltd.
Tecumseh Products Company
The Trane Company
Valeo, Inc.
Visteon Automotive Systems
Wieland-Werke, AG
Wolverine Tube, Inc.

For additional information:

Air Conditioning & Refrigeration Center
Mechanical & Industrial Engineering Dept.
University of Illinois
1206 West Green Street
Urbana, IL 61801

217 333 3115

Abstract

Scuffing as a phenomenon has been studied for many years, however, the mechanism underlying scuffing remains unexplained. Recent findings suggest that the most significant changes occur in the top 50 – 100 nm of the surface, not at the micron level as previously suggested. The goal of this study is to identify different layers and their material properties on Al390-T6 disk surface and incorporate them into a thermomechanical Finite Element model to compare with tribological testing in a High Pressure Tribometer that simulates the contact in actual air conditioning compressor surfaces.

Experimental, analytical and Finite Element studies of the nanoindentation technique are developed and used to investigate the material properties of surface layers less than 100 nm thick. All the methods are first verified in simple cases such as homogeneous materials and deposited thin film, then applied to rougher engineering Al390-T6 sample. The thin surface layers and the corresponding properties obtained from the above studies are then integrated into a thermomechanical FEM model to study the scuffing mechanism for the Al390-T6 disk and steel shoe sliding contact condition experienced in the High Pressure Tribometer that simulates realistic tribological contact in air conditioning compressor surfaces. It is shown that the FEM for nanoindentation is very useful as it is able to obtain additional properties and quantify properties of layers. It is found that a simple thermomechanical macro model does not provide sufficient information about the cause of scuffing. A FEM asperity-based micro-model is then built and successfully shows that the local contact stress and temperature increase could be extremely high under the critical loading. Also, it shows that scuffing should be a combination effect of stress and temperature increase.

Table of Contents

List of Figures

Page

List of Tables

Page

Chapter 1. Introduction

1.1 Background

Scuffing occurs in many mechanical components where sliding exists. Possibly the most accepted definition of scuffing is that set forth by the Organization for Economic Cooperation and Development (OECD), which states that "scuffing is localized damage caused by the occurrence of solid-phase welding between sliding surfaces without local surface melting" (Wear Control Handbook). In practice, when scuffing occurs, there is a sudden rise in friction force accompanied by increased noise, vibration and operating temperature. The scuffing surfaces appear as if they had been welded at discrete points. Severe wear and plastic deformation are often observed on the damaged surface. In the worst cases, this leads to seizure, which is the complete stopping of the motion, and complete failure of the components.

Scuffing as a phenomenon has been studied for many years, however, the mechanism underlying scuffing remains unexplained. Blok (1937) postulated the first ideas towards the underlying causes of scuffing. He suggested that scuffing occurs when a critical surface temperature is reached, thus lowering the shear strength of the material at the interface. Other approaches have focused on understanding the changes in the layers of fluid film that separate the contacting surfaces (Dyson, 1975; Park and Ludema, 1994). Cavatorta and Cusano (2000) studied the formation of oxides on the surface due to pressure, temperature, and relative motion and linked the presence of these protective layers to scuffing resistance.

Recently, studies have been conducted on contacting surfaces with a shoe-on-disk geometry associated with air-conditioning swash plate compressors. The analysis began with the examination of the 'simpler' unlubricated contact case (Sheiretov, 1997), and proceeded to the more realistic, starved-lubrication case (Yoon, 1999). Both the unlubricated and starved-lubricated studies attribute the occurrence of scuffing to the removal of the protective oxide film known as the transformed layer. Patel (2001) shifted the examination of changes in the subsurface at the micron-level to those that occur at the nanometer level. The chemical analysis of oxygen, carbon, aluminum and silicon concentrations showed that the most significant changes occur at depths up to 50 – 100 nm below the surface, which appears to contradict earlier studies in which the most significant layers were present at depths of several microns. Pergande (2001) successfully applied the nanoindentation technique to quantify changes in material properties of Al390-T6 samples that have undergone different levels of tribological testing. It was found that the material at the surface, and to approximately 60 nm below the surface, exhibits significantly higher hardness than the bulk material. It is also found that progressive wear of the surfaces results in a progressive weakening of the near-surface material below the surface to a depth of 60 nm, while the hardness of material below the 60 nm depth remains almost unchanged.

The present research has focused on two major goals. The first is to use analytical and FEM methods to extend the nanoindentation technique and extract more information of material properties from the nanoindentation experiments. The second goal is to integrate the information obtained by Patel, Pergande, and in this work into a thermomechanical FEM model to simulate the scuffing process. Such a study will provide a better understanding of the mechanism of scuffing.

1.2 Tribological Testing and Sample Preparation

1.2.1 Materials

The material combinations of interest in this study are Al390-T6 disks, in contact with 52100 steel shoes (See Figure 1). These materials are commonly found in automotive air conditioning swash-plate compressors. The chemical compositions of the Al390-T6 are listed in Table 1 below, obtained from the supplier, Shotic America Corporation. A relatively significant amount of silicon is added to strengthen the material.

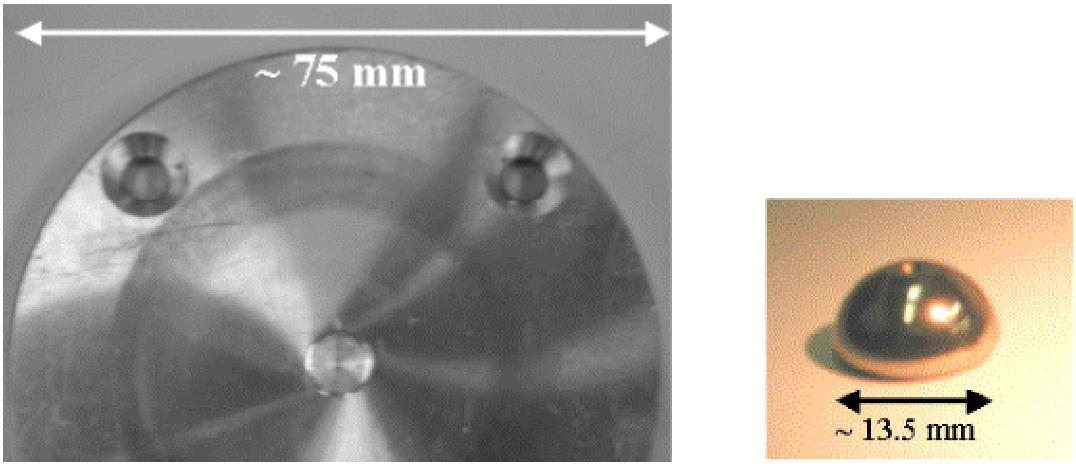

Figure 1: Al390-T6 disk sample with wear track, and 52100 steel shoe

Table 1: Al390-T6 specified alloy composition

	Al	Si	Fe	Cu	Mn	Mg
Specified weight%	Balance	16.0-18.0	<0.5	4.0-5.0	<0.1	0.45-0.65

1.2.2 Tribological Scuffing Experiments

Since this work is an extension of the analysis of the scuffing mechanism work, the samples studied are the same as Al390-T6 disks prepared from the earlier work (Patel, 2001). The High Pressure Tribometer (HPT) was used to generate worn and scuffed samples, under prescribed test conditions. The refrigerant used in this case is R410A with a POE lubricant at a supply rate of 40 mg/min to model starved lubrication conditions. The chamber pressure was set at 50 psi, while the temperature of the disks and shoes was set at 120^{o}C. These conditions model an aggressive application of a typical swash-plate compressor contact. The scuffed state occurs when there is significant material transfer from one material to the other. It is quantified by both a dramatic increase in friction, and a dramatic drop in contact resistance, as shown in Figure 2.

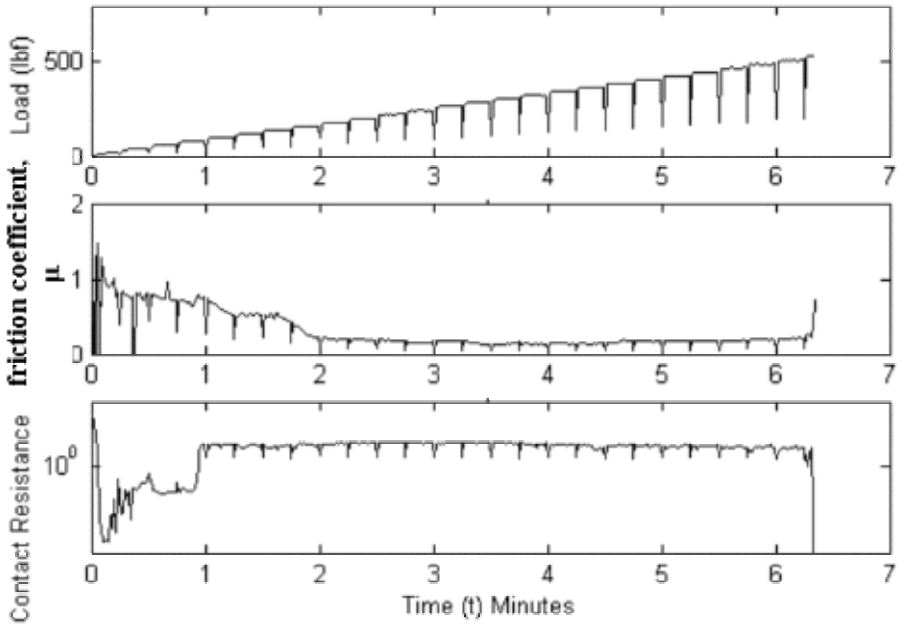

Figure 2: Typical scuffing experiment data obtained from HPT (from Patel, 2001)

1.3 Objectives

The main objective of the overall project is to investigate the scuffing mechanism. And the focus of current study is to identify different layers and their material properties on the Al390-T6 surface and integrate them into a thermomechanical Finite Element model to simulate the aforementioned tribological testing condition in HPT.

Nanoindentation experiments will be performed first on some simple cases, such as homogeneous materials and deposited thin film. Once this method is verified on these simple cases, Al390-T6 engineering surface will be studied carefully.

Alternative approaches in studying nanoindentation experiments will also be investigated. The loading curve analysis method suggested by Hainsworth et al. (1996) and the equation proposed by Johnson (1970) to relate Young's modulus, hardness and yield strength for certain materials will be tried.

A FEM model will be built to simulate the nanoindentation experiments and extract more information from the data obtained from the experiments, such as yield strength. The model will also be first verified in those simple cases then applied to the Al390-T6 sample.

Lastly, an initial thermomechanical FEM modeling work will be performed to simulate the sliding contact between Al390-T6 disk and steel shoe in the HPT. The thin surface layers and the corresponding properties obtained from previous study will be integrated into the FEM model.

Chapter 2. Nanoindentation Experiments

2.1 Background

The mechanical surface properties of many materials can be improved by depositing appropriate coatings. Particularly they can improve wear resistance, friction, and hardness. It is important to quantify the material properties of the coatings to predict and evaluate their use. Nanoindentation is one of the most successful techniques in probing the mechanical properties of materials on the sub-micron scale. The two mechanical properties measured most frequently using load and depth sensing indentation techniques are the elastic modulus, E, and the hardness H. In a commonly used procedure, data are obtained from one complete cycle of loading and unloading. The unloading data are then analyzed according to a model (e.g., Doerner and Nix, 1986), which relates the contact area at peak load to the elastic modulus. Methods for independently estimating the contact area from the indenter shape function are then used to provide separate measures of E and H.

As reported by Oliver and Pharr (1992), the effects of non-rigid indenters on the load-displacement behavior can be taken into account by defining a reduced modulus, E_r, through the equation

$$\frac{1}{E_r} = \frac{1-\nu_i^2}{E_i} + \frac{1-\nu^2}{E} \tag{1}$$

Where E and ν are Young's modulus and Poisson's ratio for the specimen, and E_i and ν_i are the same properties for the indenter. E_r is evaluated from the nanoindentation measurements according to the following equation

$$E_r = \frac{\sqrt{\pi}}{2} \frac{\left(dP/dh\right)_{unload}}{\sqrt{A_c}} \tag{2}$$

where P is the indenter load, h is the penetration depth, $(dP/dh)_{unload}$ is the experimentally measured stiffness of the upper portion of the unloading curve and A_c is the projected area of the elastic contact.

Oliver and Pharr also found that the unloading data could be described by power laws such as Equation (3) with exponents ranging from about 1.2 to 1.6. Also, the unloading contact stiffness changes continuously as the indenter is withdrawn, due to continuous changes in the contact area.

$$P = A(h - h_f)^m \tag{3}$$

In Eq. (3), A, m are the coefficient and exponent of the power law, respectively, and h_f is the residual depth as shown in Figure 3. Therefore, a least square fit to the unloading data gives the coefficients of Eq. (3), which could be analytically differentiated to determine the slope $(dP/dh)_{unload}$.

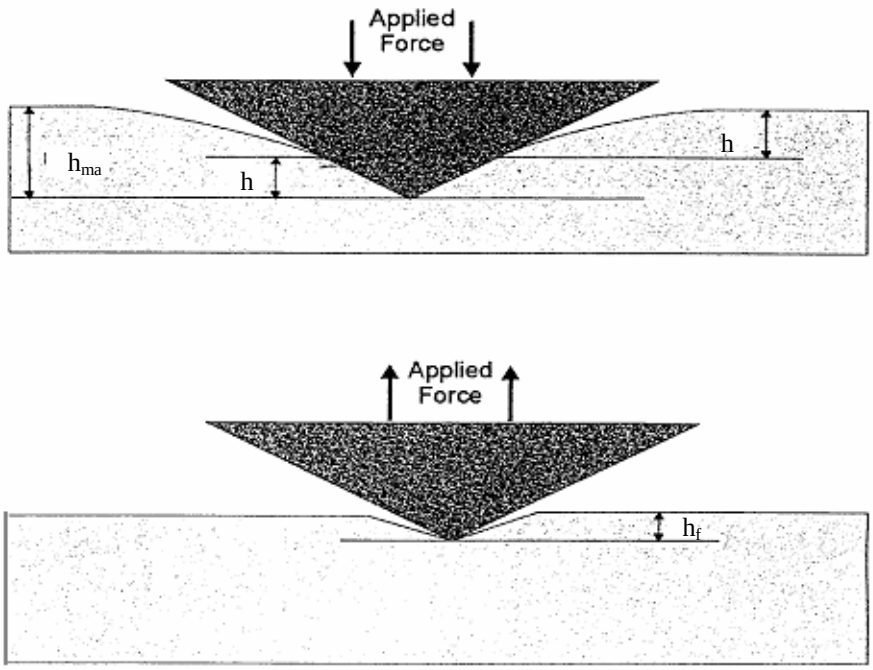

Figure 3: Cross-section profile of an ideal indentation

The contact area A_c is given as a function of the contact depth h_c. The ideal tip area function is defined as $A_c = C_0 \cdot h_c^2$, ($A_c = f(h_c)$), where C_0 is a fixed constant depending on the geometry of the tip. For a Berkovich tip, C_0 = 24.5, and for a 90 degree cube corner tip, C_0 = 2.598. In order to compensate for the finite tip radius, as well as tip manufacturing differences, additional terms are added, such that

$$A = C_0 \cdot h_c^2 + C_1 \cdot h_c + C_2 \cdot h_c^{\frac{1}{2}} + C_3 \cdot h_c^{\frac{1}{4}} + C_4 \cdot h_c^{\frac{1}{8}} + C_5 \cdot h_c^{\frac{1}{16}} \quad (4)$$

The first constant, C_0, is once again fixed depending on the geometry of the tip, while the other constants are curve fitted using a least square method on indentations carried out on a standard sample. Thus, within the calibration range, the tip contact area can be calculated based on the known contact depth, h_c. This area function is not exact, but it is a reasonable approximation.

For a specific indenter tip geometry, the contact area is precisely known, therefore the reduced modulus can be computed from Eq. (2) and the hardness is given by the well-known relation:

$$H = \frac{P_{\max}}{A_c} \quad (5)$$

Where P_{max} is the peak indention load and A_c is the contact area.

2.2 Method

Nanoindentation experiments are performed with a Triboscope Nanomechanical Testing System made by Hysitron, Inc (http://www.Hysitron.com). The Triboscope is located in the Center for Microanalysis of Materials (http://facilities.mrl.uiuc.edu/cmm/) at the University of Illinois at Urbana-Champaign. The Triboscope is an attachment to an existing Atomic Force Microscope (AFM). Hysitron's patented ultra-precision transducer technology (Bonin, 1994) adds unique capabilities to the AFM, including the capability to image the sample, choose

the test location, indent, scratch and wear surfaces. Accounting for noise, the force and displacement practical resolutions are approximately 100 nN and 0.2 nm, respectively. Based on these resolutions, the instrument is capable of indentation loads of as low as 10 μN, and displacements of less than 5 nm. The maximum load force available from the transducer is approximately 10 mN. Figure 4 shows a photograph of the nanoindentation instrument. Figure 4 (a) shows the Multimode AFM, and Figure 4 (b) shows the Triboscope transducer.

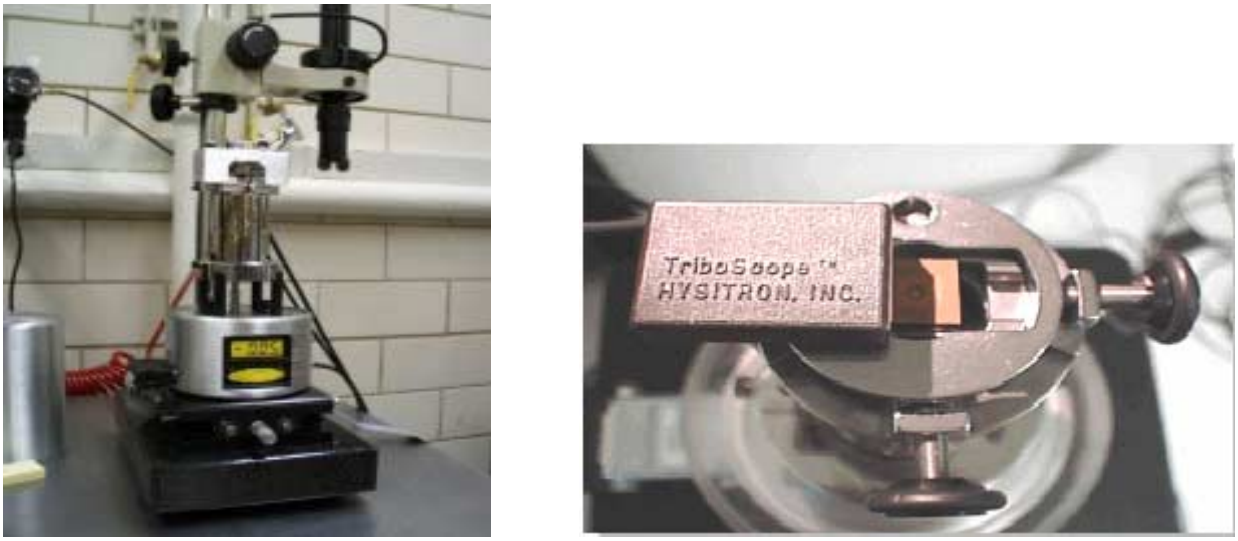

(a) (b)

Figure 4: Triboscope System on Multimode AFM: (a) Multimode AFM ;(b) Triboscope Transducer

During a continuous depth measuring nanoindentation test, a sharp tip, also referred as probe, is pushed into a sample with a known force. As the probe is pushed in, the penetration depth is also monitored. The data are collected by a data acquisition system and analyzed by the Triboscope software in a PC. The software employs the idea of Oliver and Pharr (1992) introduced in the previous section. A typical output is shown in Figure 5. All the variables discussed in the previous section such as power law coefficients, contact area, max contact load, and max depth could be found directly from the output. Based on these parameters, the reduced Young's modulus E_r and the hardness H of the sample being indented are calculated. A ramp force control loading and unloading is used for all the experiments.

The curve shown in Figure 5 represents a mechanical "fingerprint" of the sample being tested. From such a curve, one can compare the elasticity/plasticity of different materials. Also if there is an abrupt change in the slope of the loading-unloading curve, it implies a change of material (see section 2.4.2).

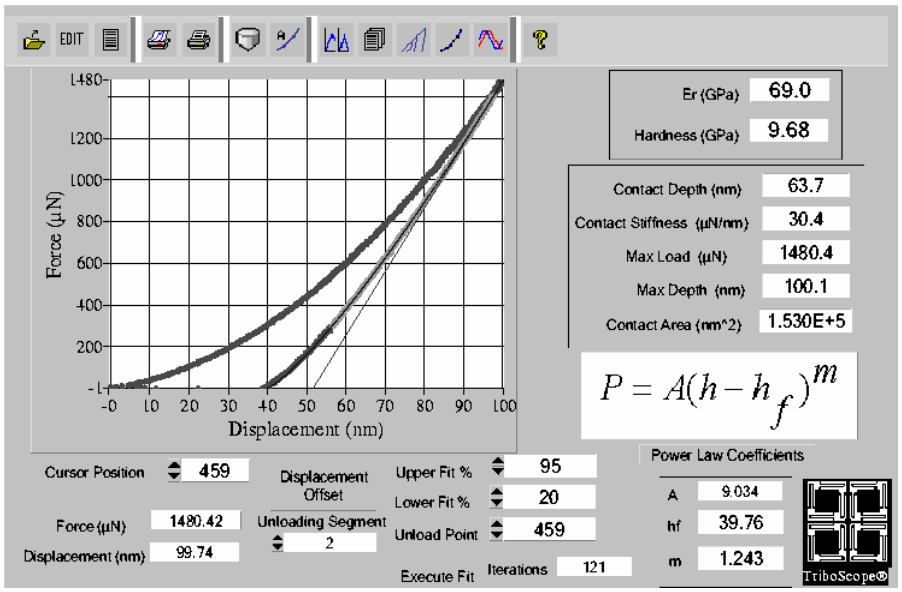

Figure 5: Typical output from the Triboscope software

The nanoindentation technique is usually used to investigate uniform smooth surfaces and thin films such as films in semiconductor and disks in hard disk drives. In this work, the nanoindentation technique is extended to more common engineering surfaces, which are usually much rougher, and nonuniform. A typical AFM image of a nanoindentation experiment on a rough surface is shown in Figure 6. A pioneering work, in which the nanoindentation technique was successfully applied on rough surfaces, was done by Pergande (2001).

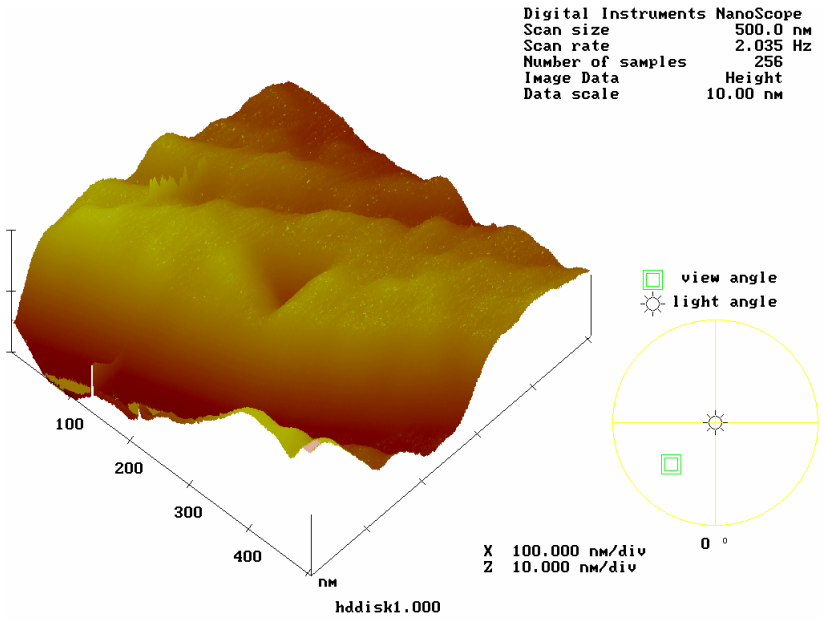

Figure 6: Residual AFM image of nanoindentation on a rough surface (image is 0.5*0.5 µm)

2.3 Tip Choice

There are many tips available for use with the Triboscope Nanomechanical Testing System. The three sided pyramid tips are the most commonly used for indentation testing on hard samples and metals. Two different kinds of pyramid tips are used for the nanoindentation experiments: a Berkovich tip and a 90 degree cube corner tip.

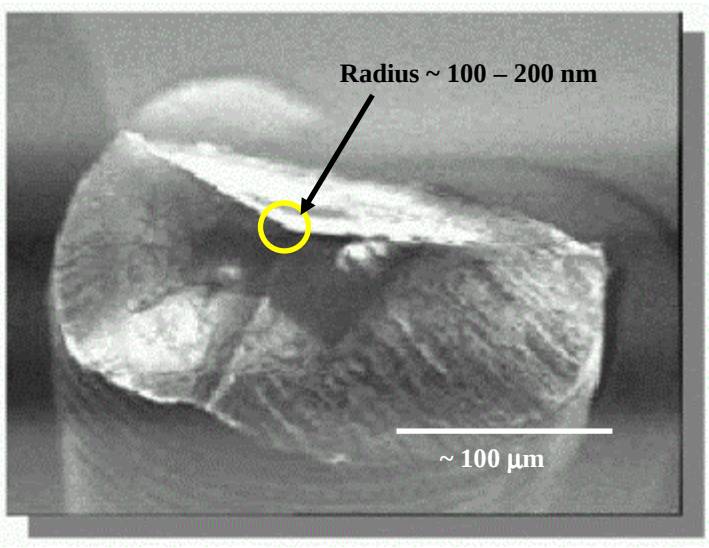

Figure 7: Berkovich tip image (from http://www.Hysitron.com)

The Berkovich tip (see Figure 7), which has been used as the "standard tip" for nanoindentation experiments, is used primarily for bulk materials and thin films with a thickness greater than 100 nm. The total included angle of the Berkovich tip is 142.3 degrees, with a half angle of 65.35 degrees. The typical spherical tip radius of curvature for a Berkovich tip is between 100-200 nm.

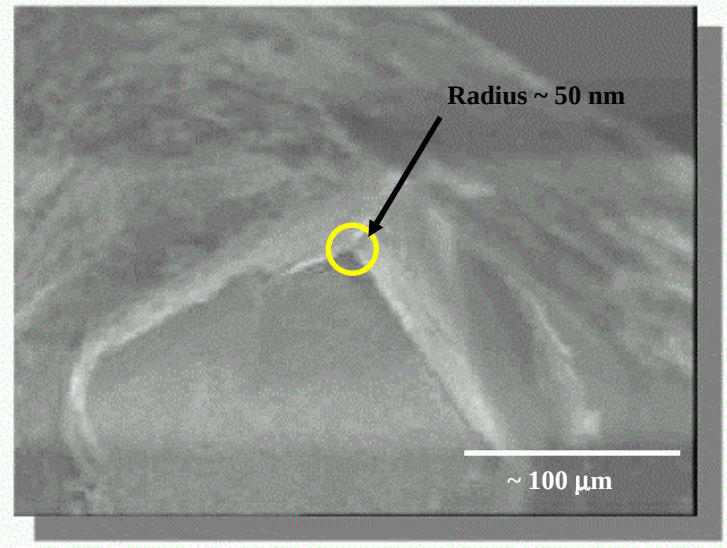

Figure 8: 90 degree cube corner tip image (from http://www.Hysitron.com)

Figure 8 shows a 90 degree cube corner tip and is used for nanoindentation experiments on ultrathin films, typically, less than 50 nm thick. The total included angle of this tip is 90 degrees, and has the same shape as the corner of a cube. The radius of curvature of this tip is usually smaller than a Berkovich tip, and is normally around 50 nm.

2.4 Nanoindentation on Homogeneous Material

2.4.1 Nanoindentation Experiments on Fused Quartz

Fused quartz is a homogeneous material with no known surface layers and is fairly smooth with $R_a < 5$ nm. Thus, fused quartz is usually used as a calibration standard for nanoindentation experiments. Accepted experimental values of the reduced modulus of elasticity and hardness are $E_r \approx 69.6$ GPa and $H \approx 9.6$ GPa, respectively. Figures 9 and 10 show typical loading-unloading curves for the 90 degree cube corner and Berkovich tips, respectively. Note that the loading curves overlap one-another, independent of the user-defined loading force and corresponding depth of indentation.

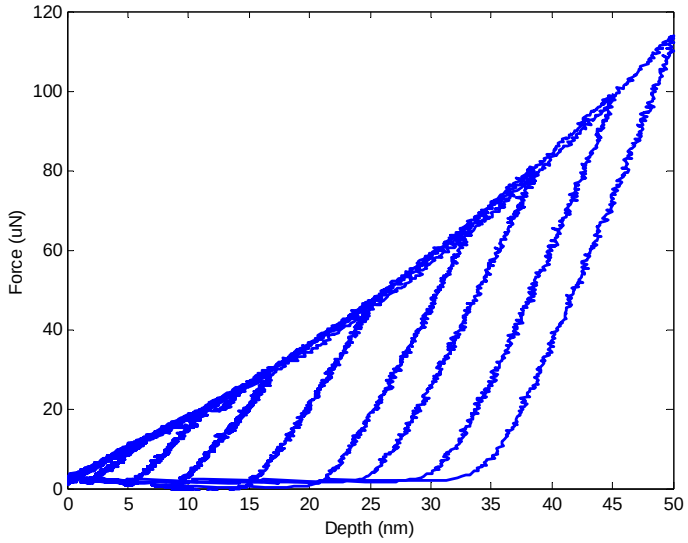

Figure 9: Fused quartz nanoindentation load-displacement curves, 90 degree cube corner tip

For each indentation experiments, the reduced Young's modulus and hardness are calculated based on the equations in section 2.1. In Figure 11, H and E_r are plotted as a function of contact depth, and it can be clearly seen that the material properties are very consistent through all the depth of the material.

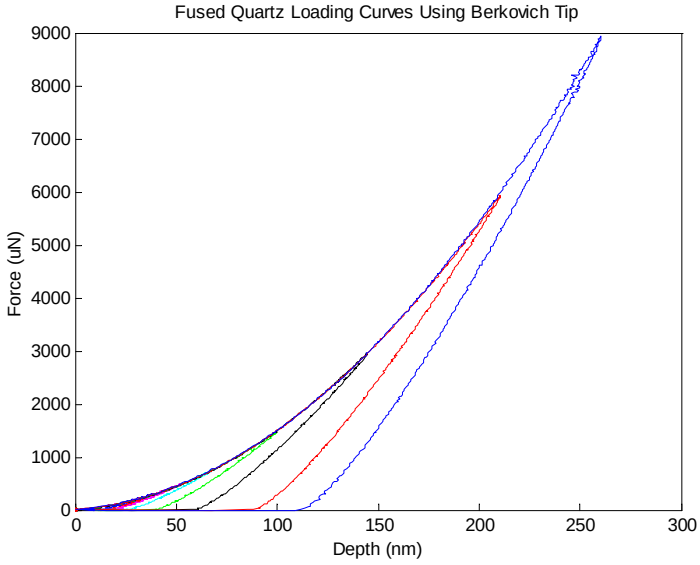

Figure 10: Fused quartz nanoindentation load-displacement curves, Berkovich tip

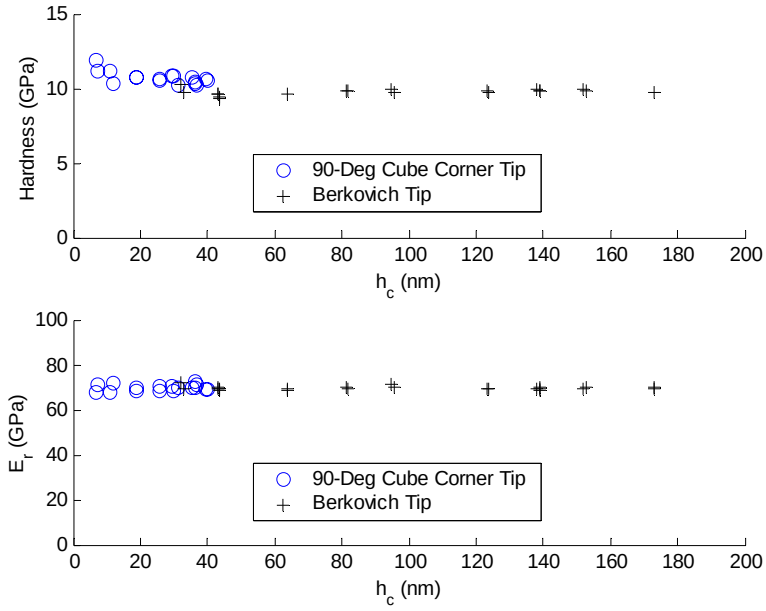

Figure 11: Fused quartz nanoindentation data

2.4.2 Nanoindentation Experiments on Silicon

Nanoindentation experiments are also performed on a silicon wafer that has an R_a < 2 nm. It is known that silicon has a very thin (~5nm) oxide layer on the surface, with the rest of the material being homogeneous. Figures 12 and 13 show typical loading-unloading curves for the 90 degree cube corner and Berkovich tips, respectively. There is a slope change around 3~5 nm of the loading curve in Figure 12, which implies the existence of the thin oxide layer on the silicon wafer. Also, note from Figure 13, that with deeper indentations silicon exhibits a large elastic recovery.

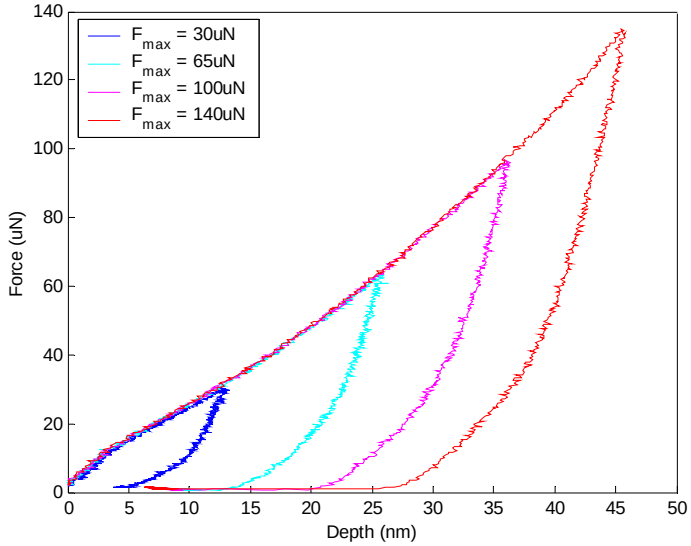

Figure 12: Silicon nanoindentation load-displacement curves, 90 degree cube corner tip

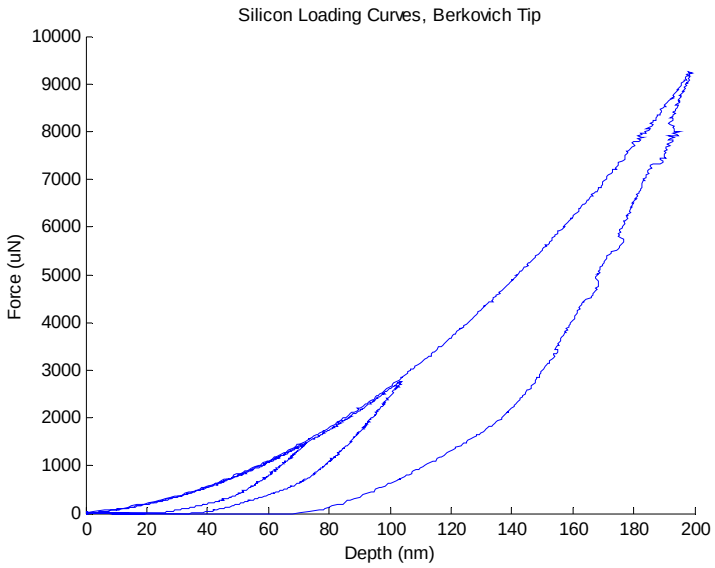

Figure 13: Silicon nanoindentation load-displacement curves, Berkovich tips

In Figure 14, H and E_r are plotted as a function of contact depth, and it can be seen that the material properties are very consistent through the depth. As the oxide layer is only 5 nm thick, the material properties of that layer could not be found by this method as its analysis is based on the loading-unloading curve around maximum displacement, and due to the limitation of the current instrument, it is impossible to get a measurement less than 5 nm deep.

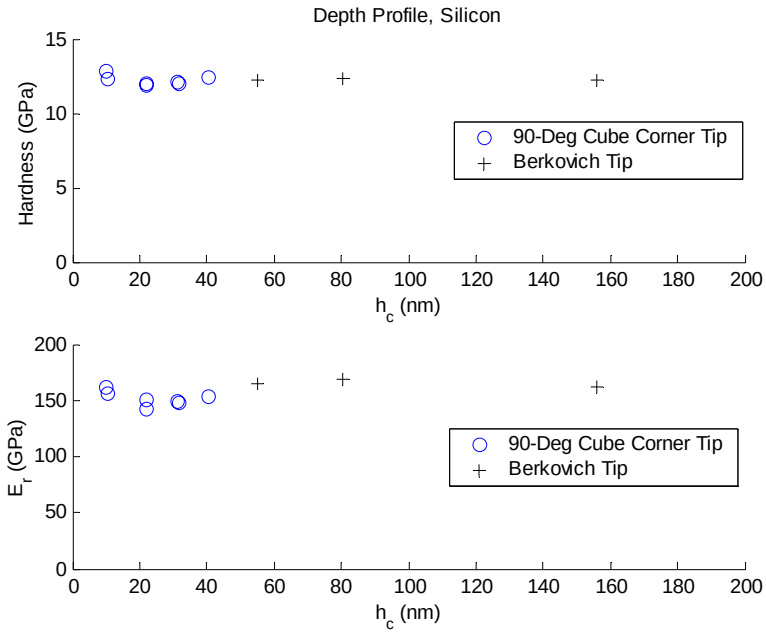

Figure 14: Silicon nanoindentation data

2.5 Deposited Thin Film: 100 nm Gold Thin Film on Silicon

The ultimate goal of this study is to employ the nanoindentation technique to rough, nonuniform engineering surfaces discussed in Chapter 1. As it will be seen in the next section, the thickness and composition of layers on the engineering surfaces are not very well known. Thus, a study on well prescribed deposited thin film for

which we know the composition and thickness will be very helpful to verify the capability of this method and bring some idea into the analysis of the actual engineering surfaces.

2.5.1 Thin-Film Deposition

Two different samples were prepared using the sputtering deposition process. The AJA Int. Co. sputtering deposition system, located in the Microfabrication Lab of the Materials Research Laboratory (htttp://www.mrl.uiuc.edu) at The University of Illinois, was used to deposit thin films on known samples. The instrument is capable of depositing thin films up to 500 nm in thickness, with an accuracy of 0.1nm. Both samples consist of 100 nm layer of gold deposited on a silicon wafer as the substrate, with a 2 nm adhesive layer between the two materials. The adhesion layer bonds the two surfaces together such that the film stays attached to the substrate material. Two different adhesion layers were used: Niobium (Nb) and Titanium (Ti). A schematic of the sample is shown below in Figure 15.

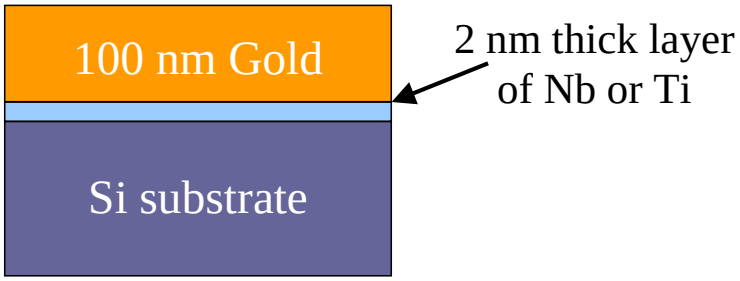

Figure 15: 100 nm gold thin film on silicon (not to scale)

2.5.2 Surface Topography Measurements

Shown below in Figure 16 is an AFM topographical image of a typical sputtered surface on a silicon wafer substrate. This image shows that deposited surfaces are much smoother than typical engineering surfaces, with R_a values of several nanometers vs. several hundreds of nanometers on engineering surfaces, as it will be discussed next.

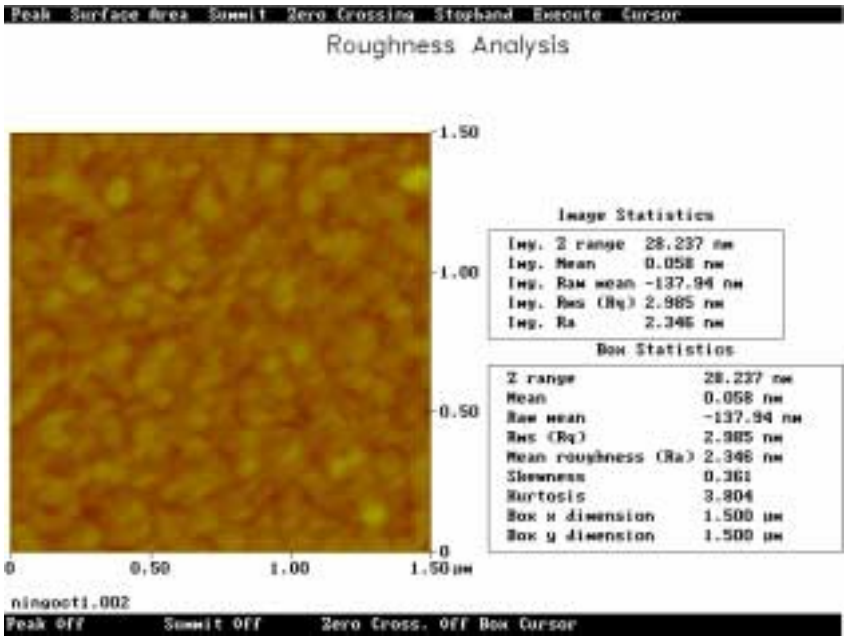

Figure 16: AFM surface topography measurement of deposited surface

2.5.3 Nanoindentation Experiments

Several indentions, of various peak loads, are performed on both samples: one with the Ti-adhesion layer and one with the Nb-adhesion layer. The results from the 90 degree cube corner and Berkovich tips indentations are shown below in Figures 17 and 18, respectively. First note the consistency in the load-displacement curves, for both tips. This is a result of a relatively smooth surface with extremely uniform layer thickness. Also note that there are no obvious differences between the loading curves of the Ti and Nb adhesion layer samples. Thus, the differences in the thin bonding layer do not significantly affect the material response to nanoindentation.

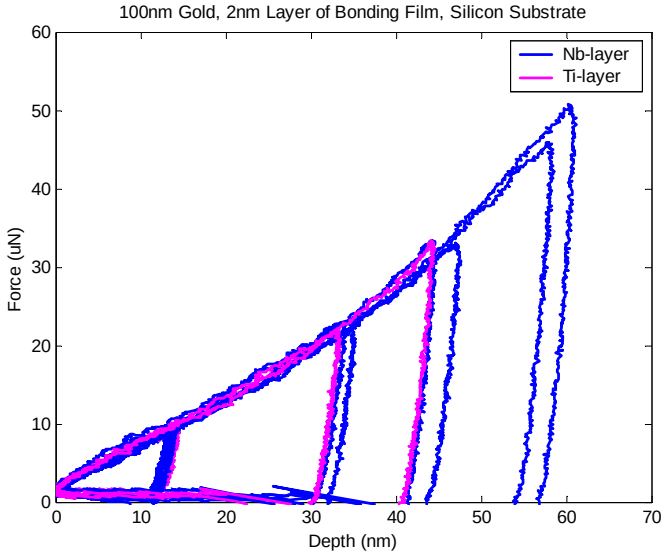

Figure 17: 100 nm Au on Si nanoindentation load-displacement curves, 90 degree cube corner tip

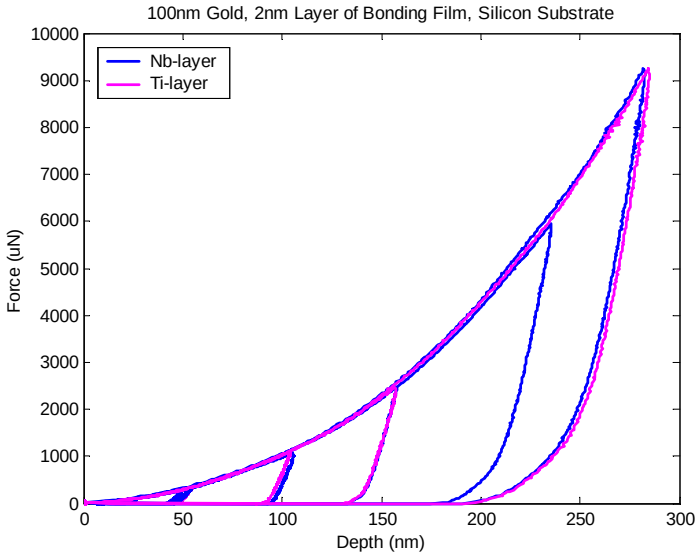

Figure 18: 100 nm Au on Si nanoindentation load-displacement curves, Berkovich tip

Shown below (Figure 19) are the calculated material properties based on the unloading curves shown in Figs. 17 and 18.

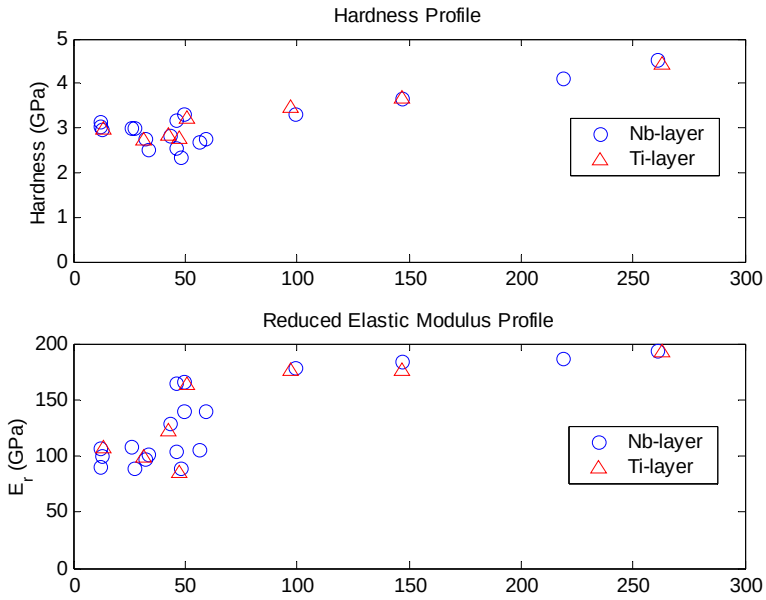

Figure 19: 100 nm Au on Si nanoindentation data

The theoretical (i.e., published) properties of bulk gold are $H \approx$ 2-3 GPa and $E_r \approx$ 94.7 GPa, and of bulk silicon are $H \approx$ 12 GPa and $E_r \approx$ 150 – 200 GPa (ASM Handbook, 1990). Thus, indentations on the surface should measure lower hardness and lower elastic modulus than those at greater depths as the substrate influence increases at greater depths. Such trend is observed on these measurements. Other researchers have shown that for an indentation to be representative only of the film material properties, irrespective of the substrate material, it must be to a depth not more than 10 – 20% of the overall layer thickness (Bhattacharya and Nix, 1988). Since the layer of gold is 100 nm thick, indentations below approximately 15 nm in depth should be representative of pure gold properties. Examination of the data shows that the hardness and elastic modulus are H ≈ 3 GPa and $E_r \approx$ 100 GPa at indentations of approximately 10 nm deep. These values are comparable to those of the pure gold sample, which is expected at very shallow indentations. Note that the reduced Young's modulus finally reaches the expected value of silicon substrate while the hardness value is still much less than the value for silicon. This is because the hardness value is greatly affected by the contact area. Since there is a soft layer on top of the silicon substrate, the contact area will be much bigger than indentations on pure silicon for the same load when the indentation depth is comparable to the thickness of the soft layer, thus, the hardness will be lower. Therefore, based on this technique, one could not obtain the hardness value of each layer in a layered material. A technique that can successfully obtain the properties for each layer is the FEM modeling, as will be discussed in Chapter 4.

2.6 Engineering Al390-T6 Sample

In this research, the ultimate goal of the nanoindentation technique is to characterize the material properties of the uppermost layers that eventually lead to scuffing (i.e. failure) for typical engineering surfaces, used in automotive air conditioning compressors. Nanoindentation experiments are done on virgin Al390-T6 surfaces, which are much rougher than the previous surfaces studied, with an R_a value of 200~300 nm. Figures 20 and 21 show some loading-unloading curves for the 90 degree cube corner and Berkovich tips, respectively. Due to the

surface roughness and the inhomogeneous nature of the Al390-T6 sample (Pergande, 2001), the nanoindentation loading-unloading curves are not as consistent as with fused quartz or silicon (see section 1.4).

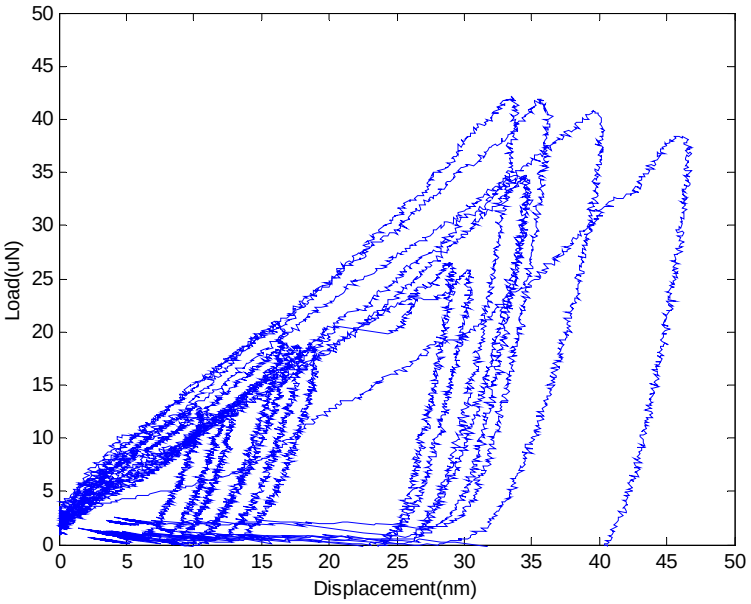

Figure 20: Engineering Al390-T6 sample nanoindentation load-displacement curves, 90 degree cube corner tip

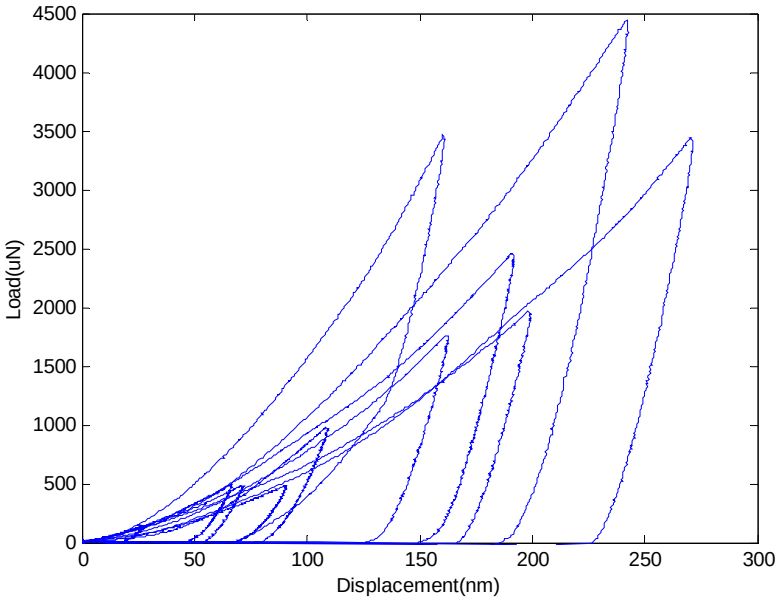

Figure 21: Engineering Al390-T6 sample nanoindentation load-displacement curves, Berkovich tip

Figures 22 and 23 plot H and E_r as a function of depth respectively. The symbols represent actual nanoindentation values, solid lines are least square fits to the data in two ranges, one from 0 to 50 nm and the other from 50 to 250 nm. The dashed lines represent the 95% confidence interval; chain lines represent the 95% prediction line (Pergande, 2001).

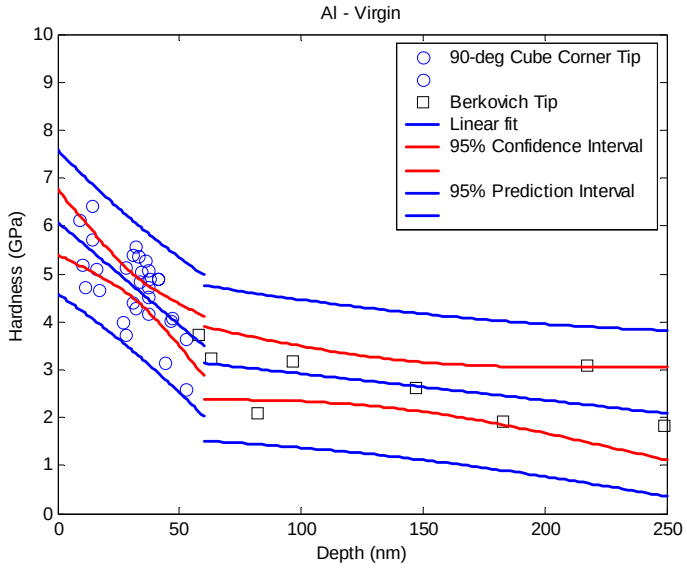

Figure 22: Engineering Al390-T6 sample hardness profile

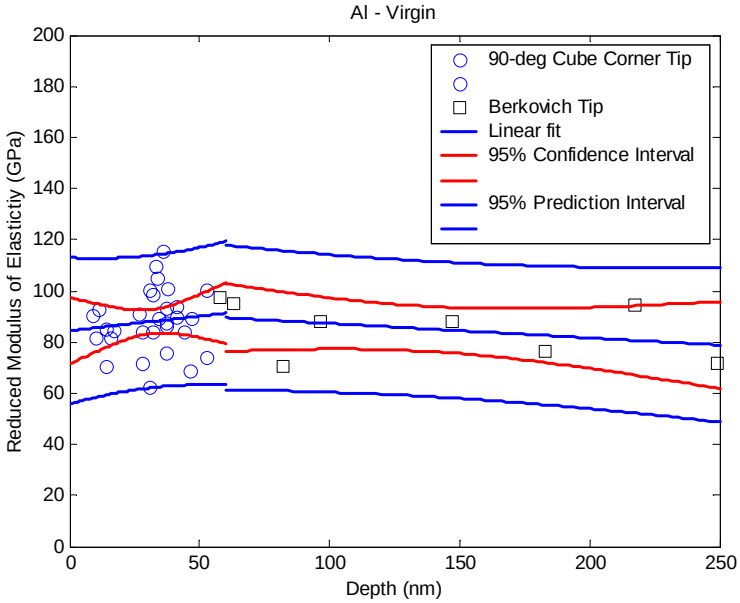

Figure 23: Engineering Al390-T6 sample reduced elastic modulus profile

Based on these results, the reduced modulus values are almost the same through all the depth while the Hardness values decrease rapidly from 6 GPa to 3 GPa in the top 50 nm, then decrease slowly and finally reach the bulk property of about 2 GPa. It could be concluded that there are several different layers on the Al390-T6 disk's surface. From the previous work by Patel (2001), it was found that the chemical composition is much different on the top 50 nm than the substrate below. Also, Pergande (2001) successfully applied the nanoindentation and nanoscratch on these engineering samples, and his work also shows the existence of such a major layer on the top. Note that in this study the nanoindentation experiments on fused quartz (section 2.4.1), silicon (section 2.4.2), and Al390-T6 (section 2.6) were performed independently and the results agree with the more extensive experiments of Pergande (2001). The results shown above in Figs. 9-14, 20-23 are from Pergande (2001) in order to enable exact comparison between the FEM work (Chapter 4) and the extensive nanoindentation experiments of Pergande (2001).

2.7 Summary

Nanoindentation experiments are performed on different homogeneous, deposited thin film, and unknown Al390-T6 surfaces. The results are consistent with the previous study by Pergande (2001). From the study of known deposited thin film (100 nm gold film on silicon), it is found that the hardness value for the multilayer surfaces is not well defined and the value itself is determined by both the top thin film and substrate material properties unless the penetration depth is very large and well into the substrate. The experiments on Al390-T6 sample show that there is a 50 nm major layer on the top that is harder than the substrate.

Chapter 3. Alternative Approaches in Studying Nanoindentation Experiments

3.1 Analysis of Nanoindentation Load-Displacement Loading Curves

3.1.1 Background

Nanoindentation loading-unloading curves represent a mechanical "fingerprint" of a material's response to contact deformation. Much attention has been focused on the unloading curve to extract the Young's modulus and hardness, as discussed in Chapter 2. However, if the test volume displays considerable elastic recovery when the load is removed, e.g., for many stiff hard materials and many inhomogeneous systems (e.g., those employing thin hard coatings), then the unloading curve does not fit existing models particularly well (Doerner and Nix, 1986).

An alternative approach, based on the analysis of the loading curve of a loading-unloading nanoindentation experiments instead of the unloading curve, has been suggested by Hainsworth et al. (1996). Starting from the assumption that the total deformation can be decomposed into a plastic and an elastic part, they derived a relationship between the applied load, P and *in-situ* displacement, h of the loading curve as:

$$P = E\left(\phi\sqrt{\frac{E}{H}} + \psi\sqrt{\frac{H}{E}}\right)^{-2} h^2 = K_m h^2 \qquad (6)$$

The first part of the equation corresponds to the elastic contribution and the second part to the plastic. The indenter constants ϕ and ψ are experimentally determined, and are valid for a wide range of materials. The value of ϕ and ψ change for different indenter geometry.

The value of K_m from the model can then be compared directly with an experimentally determined value $K_{\exp} = P/h^2$, and if either E or H is known, the other (E or H) can be calculated. Note that unlike Oliver and Pharr's method discussed in Chapter 2 that one can obtain both E and H from a single experiment (unloading curve), in this method, one needs to know one of the material property to obtain the other.

For a coated material, by using Eq. (6), the shape of the P vs. h^2 could be predicted as illustrated in Figure 24. Initially, the loading curve follows a straight line if plotted as P vs. h^2. In this range, called region I, the substrate is not influencing the response. The slope of the curve would be predicted by E and H of the coating only, according to Eq. (6). When the load is further increased, not only the coating will deform but also the substrate and interface region. Therefore a more complex shape of P vs. h^2 curve can be expected, which does not necessarily follow a straight line (region II). For even higher displacements (region III), the substrate would mainly carry the load, and a straight line predicted from E and H of the substrate should be observed as shown in Figure 24.

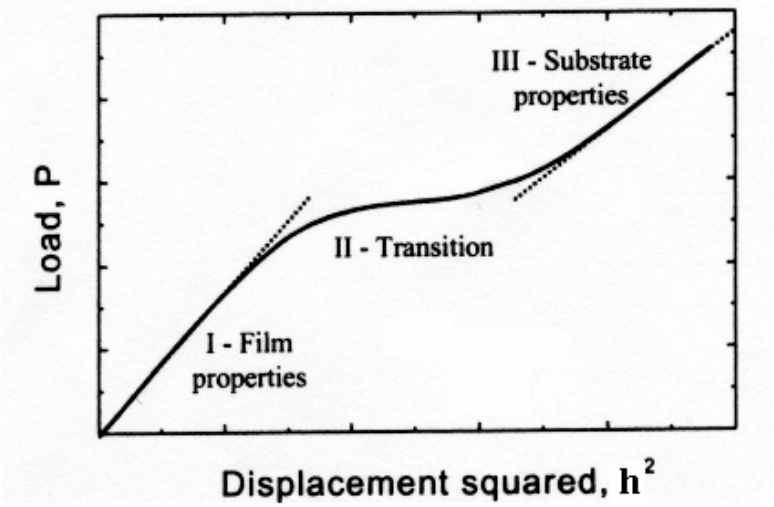

Figure 24: The predicted P vs. h^2 relationship for coated materials (from Hellgren, 1999)

3.1.2 Homogeneous Material

The fused quartz sample is first studied to verify the linear relationship between P and h^2 for a homogeneous material. Since the loading parts of all the fused quartz indentations are very consistent as it was shown in Figs.9 and 10. Thus, a 105 μN nanoindentation experiment with a maximum depth of 45.6 nm is selected to represent the 90 degree cube corner tip nanoindentations while a 1,500 μN nanoindentation with a maximum depth of 100.07 nm is selected to represent the Berkovich tip nanoindentations.

Figures 25 and 26 plot the P vs. h^2 for the 90 degree cube corner and Berkovich nanoindentations, respectively. For both figures, it could be seen that the curves show a perfect linear relationship after the initial segment. The initial nonlinear segment is due to the radius of curvature on both tips. As it was also pointed out in (Hainsworth et al., 1996), the linear relationship between P and h^2 does not hold for spherical indenters, thus the nonlinear initial part on homogeneous material could be reasonably explained. Based on the fitting in Figs. 25 and 26, the effect of the top spherical shape affect the P vs. h^2 relationship up to depths of h =20 nm and 40 nm for the 90 degree cube corner and Berkovich indenter, respectively. These two numbers will also be used for the more complex deposited thin film and rough engineering samples.

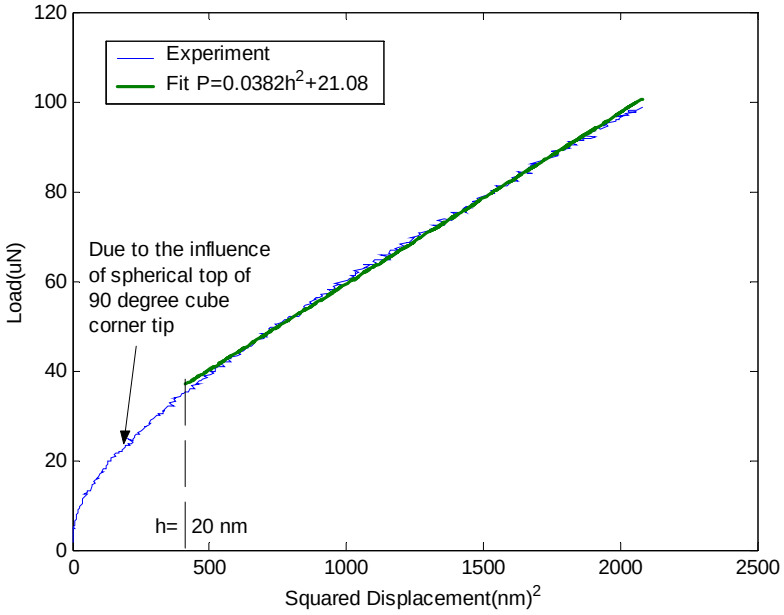

Figure 25: P vs. h^2 for 90 degree cube corner tip nanoindentation on fused quartz

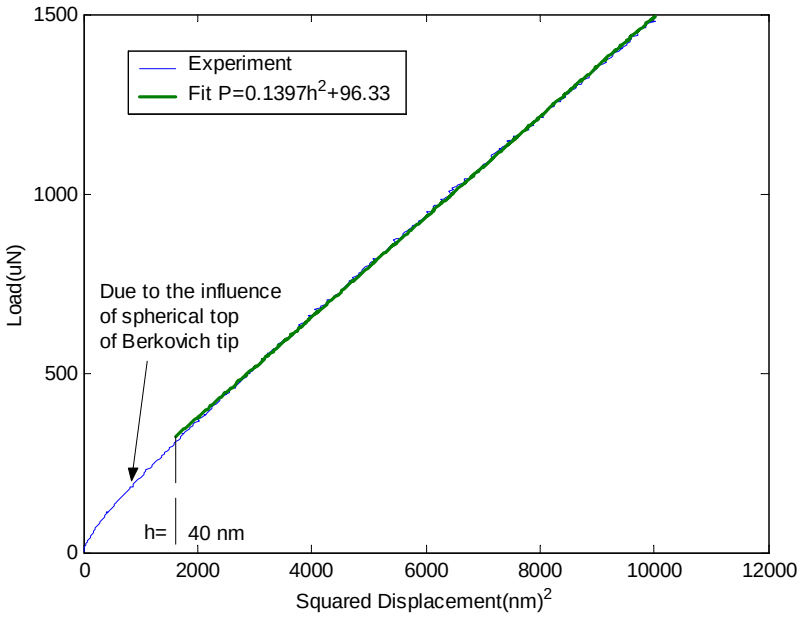

Figure 26: P vs. h^2 for Berkovich tip nanoindentation on fused quartz

Next, the P vs. h^2 relationship is also checked with silicon. A 100 μN cube corner tip nanoindentation experiment with a maximum depth of 36.4 nm is selected to represent the 90 degree cube corner tip nanoindentation and a 2,800 μN nanoindentation experiment with a maximum depth of 103.8 nm is selected to represent the Berkovich tip. Figures 27 and 28 show the P vs. h^2 curves for 90 degree cube corner and Berkovich tips, respectively.

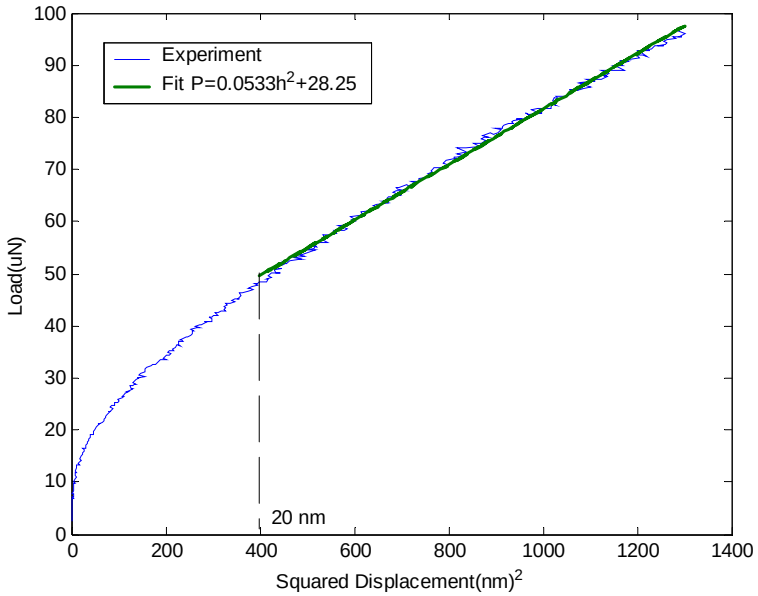

Figure 27: P vs. h^2 for 90 degree cube corner tip nanoindentation on silicon

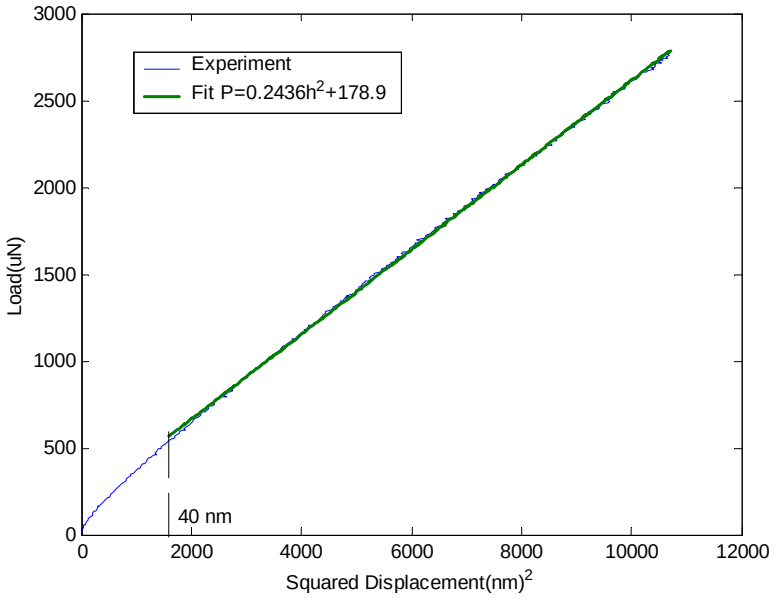

Figure 28: P vs. h^2 for Berkovich tip nanoindentation on silicon

As with fused quartz, the linear relationship between P and h^2 is still valid for both 90 degree cube corner and Berkovich nanoindentation experiments.

Based on the above results on fused quartz and silicon, one can now calculate the two constants ϕ and ψ in Eq. (6) for each tip geometry.

For fused quartz, from nanoindentation experiments discussed in section 2.4.1, we get an average reduced modulus, E_r = 69.6GPa, therefore, according to Eq. (1),

$$\frac{1}{E_r} = \frac{1-0.07^2}{1140} + \frac{1-0.17^2}{E} \Rightarrow E = 72GPa$$

Thus, the Young's modulus of the measured fused quartz sample is 72GPa, which agrees with the value in (ASM Handbook, 1990). The measured hardness, H = 10 GPa (average of the 90 degree cube corner and Berkovich results).

For silicon, the average reduced Young's modulus is found to be 165.6 GPa. Therefore

$$\frac{1}{E_r} = \frac{1-0.07^2}{1140} + \frac{1-0.278^2}{E} \Rightarrow E = 178.6GPa$$

Thus, the Young's modulus of the measured silicon is 178.6 GPa, which agrees with the value in (ASM Handbook, 1990). The measured hardness, H = 12 GPa.

Substituting the material properties and the experimental slope into Eq. (6),

$$\begin{Bmatrix} K_{\exp-si} = K_{m-si} = E_{si}\left(\phi\sqrt{\frac{E_{si}}{H_{si}}} + \psi\sqrt{\frac{H_{si}}{E_{si}}}\right)^{-2} \\ K_{\exp-fused} = K_{m-fused} = E_{fused}\left(\phi\sqrt{\frac{E_{fused}}{H_{fused}}} + \psi\sqrt{\frac{H_{fused}}{E_{fused}}}\right)^{-2} \end{Bmatrix}$$

the experimental slope K_{exp} for different materials and different indenters are found by least square fit on the P vs. h^2 curves, and the values are indicated in Figs. 25-28. Thus, the two unknown ϕ and ψ could be solved from above two equations for 90 degree cube corner and Berkovich tips, respectively.

The results are listed in Table 2.

Table 2: Indenter Constant ϕ and ψ for different tip geometry

	ϕ	ψ
90 degree cube corner tip	0.440l	0.509
Berkovich tip	0.179	0.636

3.1.3 Deposited Thin Film: 100 nm Gold Thin Films on Silicon

Next, the controlled deposited thin film samples discussed in Chapter 2 are used to study the P vs. h^2 capability for layered material. A 27 μN nanoindentation experiment with a maximum depth of 34.8 nm is selected to represent the 90 degree cube corner tip and a 2,500 μN nanoindentation with a maximum depth of 157.6 nm is selected to represent the Berkovich tip experiments.

Figures 29 plots the P vs. h^2 for the aforementioned cube corner tip nanoindentation experiment.

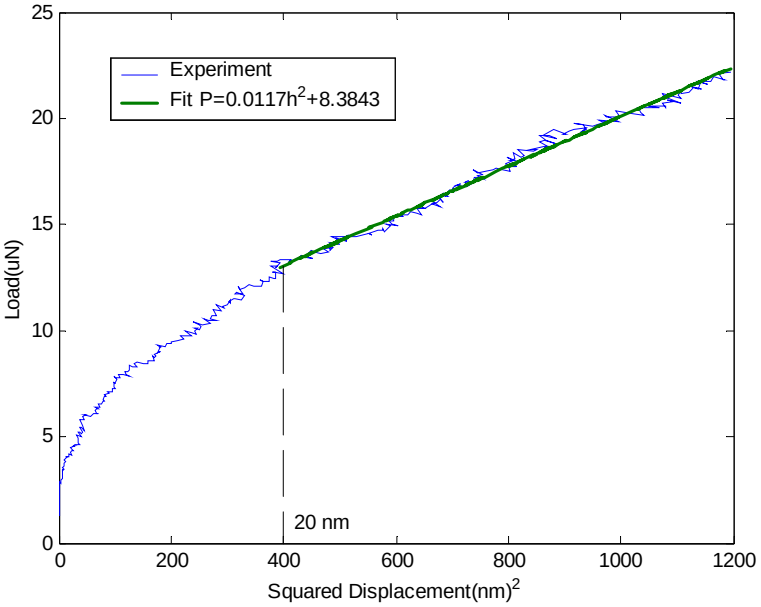

Figure 29: P vs. h^2 for 90 degree cube corner tip nanoindentation on 100 nm Au on Si sample

It could be seen that as in Figs. 25 and 27, the P and h^2 linear relationship holds, except for the initial segment due to the spherical top of the indenter. It was found from the experiments that the average reduced Young's modulus for the gold coating is 99.2 GPa. Therefore, the Young's modulus could be found by

$$\frac{1}{E_r} = \frac{1-0.07^2}{1140} + \frac{1-0.42^2}{E} \Rightarrow E = 89.4GPa$$

and the measured hardness for a gold film is 3 GPa. Using ϕ and ψ for cube corner tip found earlier, we can then use Eq. (6) to obtain the theoretical slope K_m = 0.0143. Comparing it with the actual slope for Figure 29, there is a 22% relative error between the theoretical prediction and experimental determined slope. This may be caused by the inexact evaluation of the gold film properties due to the instrument limitations as discussed in Chapter 2. Also note that according to (Hainsworth et al., 1996), silicon's curve does not fit Eq. (6) as well as many other materials because it is known to undergo a pressure-sensitive phase transformation. Due to the limitation of available samples, the constants for Eq. (6) in this work are derived from the curves from the nanoindentation on fused quartz and silicon; a further study on many other materials will probably give a better evaluation of the two constants.

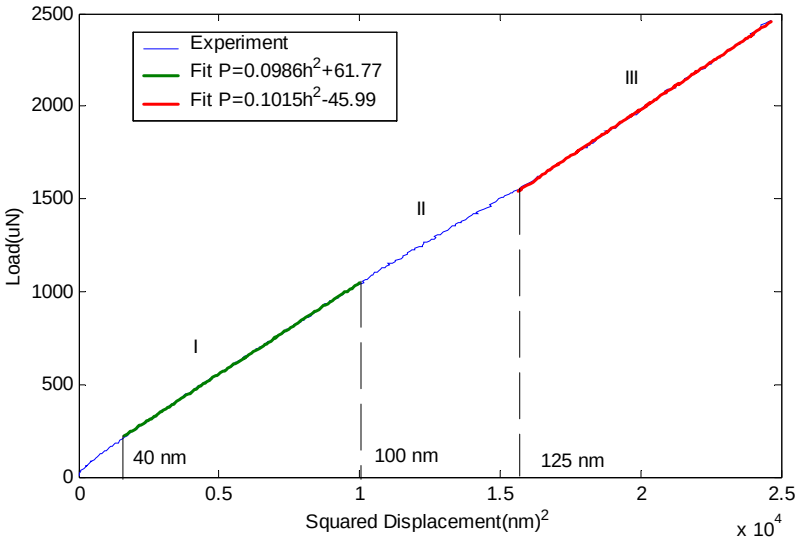

Figure 30: P vs h^2 for Berkovich tip nanoindentation on 100 nm Au on Si sample

Figure 30 plots the P vs. h^2 for the aforementioned Berkovich tip nanoindentation experiments. Up to h= 40 nm, the nonlinearity is due to the tip spherical shape. From h = 40 nm to h=100 nm, there is a linear segment and the slope is 0.0986. Assume that the slope of the first linear segment is determined by the gold properties, from Eq. (6), the theoretical prediction of the slope is 0.0746, compared to experimental value of 0.0986, once again, there is a 24% error. Also, although the substrate data do fall in a linear line after h = 125 nm, the slope is 0.101, which is only half the value as the slope we see for the pure silicon (see Figure 28). It is opposite to the claim in (Hainsworth et al., 1996) that the curve in the second linear segment is determined by the E and H value of the substrate only and it may due be to the fact that to obtain the correct H for substrate, really deep indentation need to be done as seen in section 2.5. There is a change in slope, which happens around 100 nm (the thickness of the gold film), but the change is really not so obvious as described in the schematic of Figure 24.

In general, the prediction of the slope by Eq. (6) seems not to be good for predicting the E and H values, which could be improved by using more material other than fused quartz and silicon to get more accurate indenter constants ϕ and ψ.

The slope changes in linear relationship could help on identifying out the thickness of different layers. However, the results need to be considered carefully and compared with other methods.

3.1.4 Engineering Al390-T6 Sample

The ultimate goal of this study is to help identify the different layers on the Al390-T6 sample. As discussed in Chapter 2, based on the chemical analysis of the surface, it is suggested that there are a 50 nm thick major layer on top of the surface. As the loading-unloading curves for the Al390-T6 sample are not as consistent as the previous samples, a median experiment was selected for the 90 degree cube corner and Berkovich nanoindentations, respectively, and considered to represent the average material properties best.

Since the main interest is the top 50 nm, the Berkovich nanoindentation experiment is first studied here. Figure 31(a) plots the P vs. h^2 for Berkovich indentation, and Figure 31(b) is a zoom-in graph for the range h^2 up to 12,000 nm^2. Note that from previous P vs. h^2 relationship for Berkovich indentation, the nonlinear segment due to the tip blunting always ends before 40 nm, thus the first linear segment in that graph is a valid one. The transition

depth between two linear segments is between 67.5 nm to 80 nm, which corresponds to the estimation of the major layer quite well.

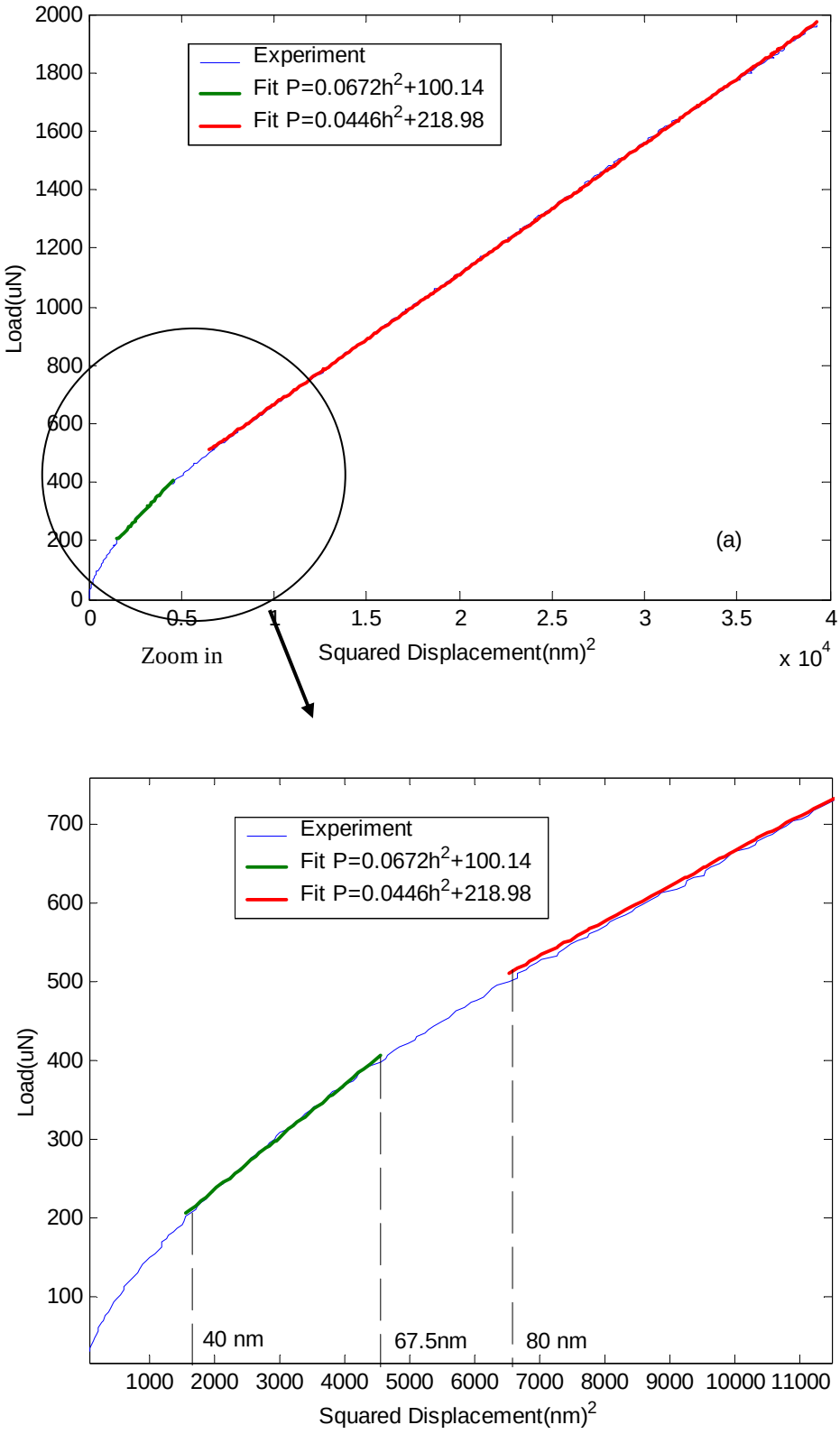

Figure 31: P vs h^2 for Berkovich tip nanoindentation on engineering Al390-T6 sample

The average E_r for the top 50 nm nanoindentation is 88.5 GPa, while average E_r for the substrate below is 88 GPa. The Poisson's ratio is taken as the standard value for aluminum, i.e., 0.33.

$$\frac{1}{E_r}=\frac{1-0.07^2}{1140}+\frac{1-0.33^2}{E}\Rightarrow\begin{cases}E_{top50nm}=85.5GPa\\E_{substrate}=84.9GPa\end{cases}$$

And the hardness for the top layer and substrate are 5 GPa and 3 GPa respectively, as measured using unloading curve (see section 2.6). Using Eq. (6), the theoretical slope prediction for the top layer and substrate are 0.107 and 0.074. Again, there are relatively big errors in the slope prediction, but the trend of decreased slope is predicted correctly. Note that strictly speaking, Eq. (6) holds only for homogeneous materials (fused quartz, and silicon) or one layer's behavior is dominant (shallow indentation on the 100 nm gold film).

Figure 32 plots the P vs. h^2 for 90 degree cube corner indentation. It can be seen that there may exist several sub layers. A more careful study needs to be done before any definite conclusion may be reached on the detailed structure for these sub layers.

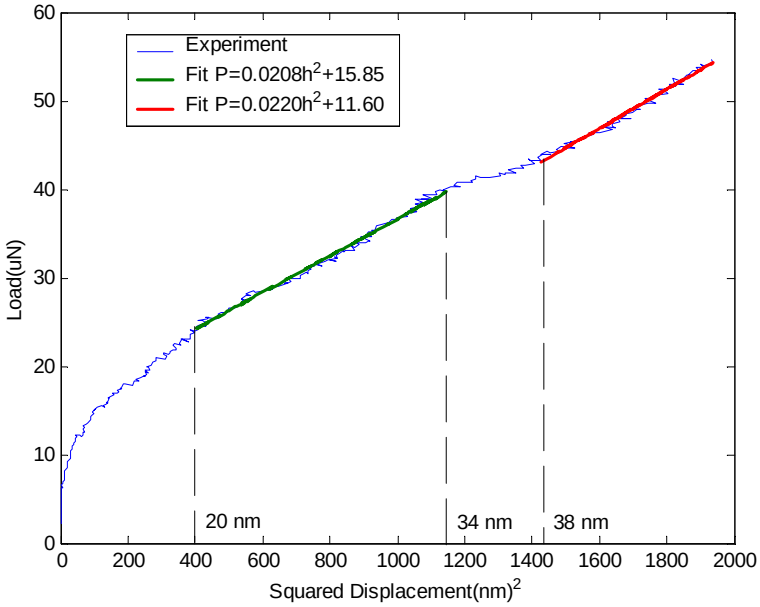

Figure 32: P vs h^2 for 90 degree cube corner tip nanoindentation on engineering Al390-T6 sample

3.2 Yield Strength from Hardness Measurements

3.2.1 Background

Once the value of E and H are obtained from nanoindentation, typically one needs to know the yield strength, Y of the material as well. One could use one of the two methods to obtain Y: analytical methods such as Equation (7) and (8)-(9) below, or numerical method such as FEM as it will be discussed in Chapter 4.

For ductile materials, Tabor (1951) has shown that the hardness (or mean contact pressure), can be related to the yield stress of the material, Y in simple compression, by an expression based on the theory of indentation of a rigid perfectly-plastic solid,

$$H=CY \tag{7}$$

where *C* is a constant whose value is about 3, depending to some extent upon the geometry of the indenter. For ductile materials and other similar materials, this relationship works well.

Contrary to ductile materials, indentation experiments with highly elastic materials, such as polymers, have shown that the elastic and plastic strains associated with indentation are of the same order of magnitude and the above relationship does not apply. Johnson (1970), using Marsh's (1964) model of the expanding spherical cavity in an elastic-perfectly plastic solid, derived a comprehensive relationship between the hardness, yield strength, Young's modulus and the indenter shape defined by the angle β between the indenter and the horizontal as shown in Figure 33.

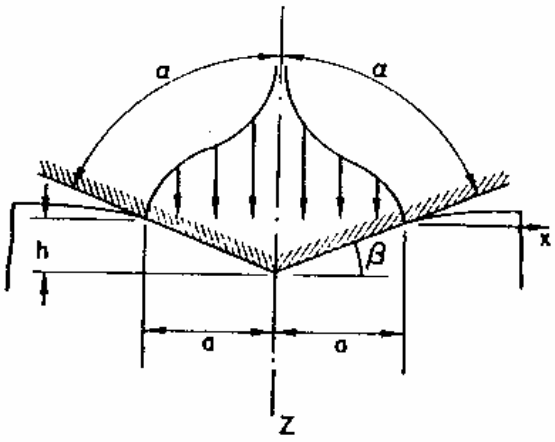

Figure 33: Indentation of a surface by a rigid cone (from Johnson, 1970)

For a pyramid indenter, β is taken to be the equivalent angle for a cone which displace the same volume of material (19.7° for Berkovich and 47.7° for 90 degree cube corner tip). For a rigid cone, the mean pressure (hardness) in the cone, $\overline{p}$ is given by

$$\frac{H}{Y} = \frac{\overline{p}}{Y} = \frac{2}{3} + 2\ln\left(\frac{c}{a}\right) \tag{8}$$

where *a* is the contact semi-width, *c* is the radius of the elastic-plastic boundary, which is located by

$$\frac{E}{Y}\tan\beta = 6(1-\nu)\left(\frac{c}{a}\right)^3 - 4(1-2\nu) \tag{9}$$

Therefore *E*, *H* and *Y* are related in Eqs. (8) and (9). By knowing two of the properties, the third one could be readily obtained. Note that the equations only hold for small strains, and hence for small β, typically less than 30° (Johnson, 1970). Therefore, Eqs. (8) and (9) are only applicable for the Berkovich tip indentation results, and not the 90 degree cube corner results.

3.2.2 Application to this work

From the nanoindentation experiments described in Chapter 2, we already have the Young's modulus and hardness. Thus, the yield strengths are estimated using both methods described above and the results are listed in Table 3. The FEM results from Chapter 4 are also listed in the same Table and are considered to represent the "correct" values. Note that this simple analytical method only works for homogeneous materials, for the deposited

thin film and engineering Al390-T6 sample, the material properties measured from deep Berkovich nanoindentation experiments are used here to get an estimate of the yield strength.

Table 3: Yield strength from Berkovich nanoindentation measurement

(GPa)			
	Eq. (7)	**Eqs. (8) and (9)**	**FEM (Chapter 4)**
Fused Quartz ***E*=72; *H*=9.6; *v*=0.17**	3.20	18.05	4.2
Silicon ***E*=178.6; *H*=12; *v*=0.278**	4.00	12.08	4.3
100 nm Au on Silicon ***E*=178.6;*H*=4; *v*=0.278**	1.33	1.32	Top: 0.80 Substrate: 4.30
Engineering Al Sample ***E*=84.9;*H*=3; *v*=0.33**	1.00	1.79	Top50nm: 1.80 Substrate: 1.10

From the nanoindentation loading-unloading experiments, we observe that there is always considerable elastic recovery for all the Berkovich tip nanoindentation experiments. Thus, theoretically, Johnson's equations should give a better estimation than Tabor's method.

From the results shown in Table 3, neither method gives good estimate of the yield strength. This is not surprising since the two homogeneous materials used (fused quartz and silicon) are very brittle materials, which violate the assumptions of both methods. Also these methods work only for homogeneous materials.

It is worth noting that this method seems to give more reasonable estimate for the rough engineering Al sample, which may be due to the fact that its material properties are not as brittle as the other ones. Future work needs to be done on homogeneous, more plastic materials like gold, copper, or steel to further investigate this method. Such an approach, if successful, could be very valuable, since it gives a direct method to calculate the yield strength of a material without performing the more tedious FEM simulation.

3.3 Summary

Alternative approaches in studying the nanoindentation experiments have been tested. It is found that the load, P, vs. the square of penetration depth, h^2, linear relationship works quite well in identifying different layers and their thickness. However, the prediction of the slope of P vs. h^2 still has an error of about 25% and maybe improved by studying other homogeneous materials to obtain more accurate indenter constants. The Johnson's equation that relates the yield strength to measured Young's modulus and hardness is also used and although the results deviate somewhat from later more accurate FEM work, it still seems to be valid for certain materials, such as ductile metals.

Chapter 4. Finite Element Analysis of Nanoindentation

4.1 Background

Nanoindentation experiments were performed to determine the Young's modulus and hardness of different homogeneous, deposited thin film and unknown engineering surfaces as discussed in Chapter 2. However, there are several limitations of a purely experimental approach, as described below.

First, purely experimental work cannot determine the value of yield strength of materials. As discussed in Chapter 3, hardness is not a very well defined material property as its value depends on the method that it is measured, i.e., even for the same homogeneous material, the hardness value will be different if measure using different tips. For example, for fused quartz sample, after tip area calibration, the average hardness value for Berkovich tip is 9.6 GPa while the value for 90 degree Cube corner is 10.5 GPa. Therefore, the yield strength is more preferable when one discusses the strength of the material and is much more useful for further analysis (see Chapter 5), as it is a standard parameter for many models.

Second, for samples with thin coatings, the measured Young's modulus and hardness are the combined effects of all the layers. It is really hard to determine the material properties of each layer, especially the hardness, from the nanoindentation experiments. As seen in section 2.5, for the case of 100 nm gold thin films on silicon, the hardness value is far below the expected value of silicon, even though when the indentation depth is certainly in the silicon substrate.

Third, as mentioned in Chapter 2, a rule of thumb is that to obtain the material properties of the top layer without any effects from the substrate, one should only make indentations less than 10% of the layer's thickness. This means that for existing nanoindentation techniques, we really have no means to obtain material properties for the top 50 nm layer since instruments are incapable of nanoindentation less than 5 nm deep.

The Finite Element method could help extract more information from the experimental results of nanoindentation, and overcome all the limitations mentioned above. A first example of comparison between FEM and experimental results was presented by Bhattacharya and Nix (1988) in which they simulated a sub-micrometer indentation test. Their results demonstrated that it is possible to extract the Young's modulus, E, and hardness, H from the slope of the linear portion of the unloading curve and from simulated data along the loading curve, respectively. Edlinger et al. (1993) described in detail the numerical treatment of contact conditions and the influence of friction between a rigid indenter and the indented surface in a typical nanoindentation experiment. A lot of researchers further developed the FEM method to investigate the material properties of thin films, such as the work done by Lichinichi el al. (1998) and Ma et al. (1998).

4.2 FEM Model

Simulations of the nanoindentation process are performed using the large strain elasto-plastic feature of the ABAQUS finite element code, with uniaxial stress-strain data as an input. The indenter and specimen are treated as bodies of revolution to avoid the inherent three-dimensional nature of the problem of indentation with a pyramidal shaped indenter. Lichinichi et al. (1998) have shown that there are no significant differences between the axisymmetric model with a conical indenter and the three-dimensional pyramidal model.

The pyramidal indenter is approximated by an axisymmetric cone of equal volume for a given indenter depth. The indenter is first assumed to be perfect as also assumed by Bhattacharya and Nix (1988). Later in this chapter it will be shown that for both 90 degree cube corner and Berkovich tips, the radius on the tip must also be

considered. The indenter and the specimen are shown in Figure 34 with the appropriate boundary conditions for the problem.

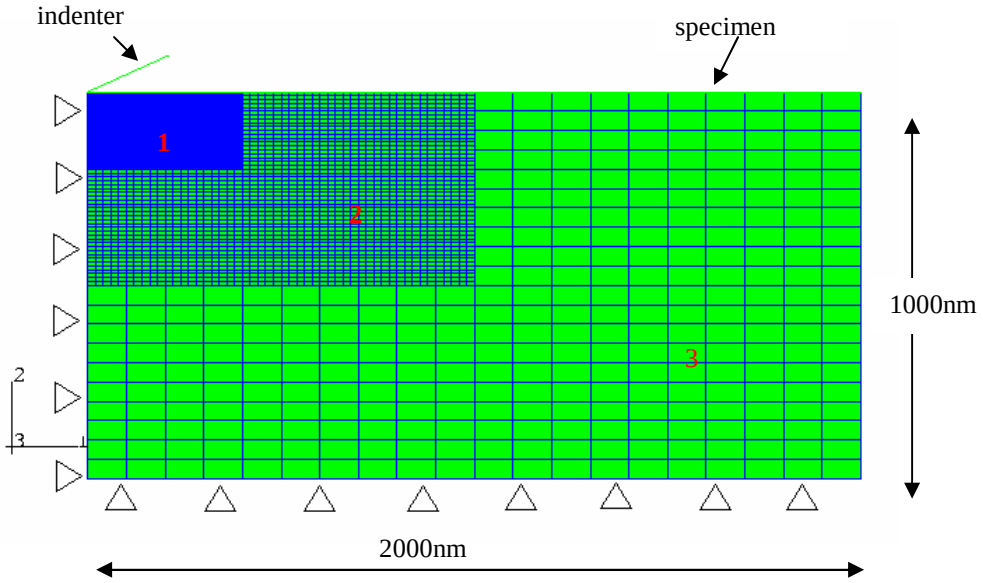

Figure 34: Finite Element Model

For this study, the indenter is considered to be rigid since the diamond tip is extremely rigid, with E_i = 1,140 GPa and ν_i = 0.07, respectively. The material behavior of the specimen is taken as elastic fully plastic and also assumed to be initially stress free.

An important feature of ABAQUS is its capability to model the contact between the indenter and the specimen as a sliding interface. From the initial geometry the nodal gap between the surfaces are defined. During the analysis, the program controls the variation of the nodal gap. In particular whenever the distance between the indenter and the specimen becomes zero-gap closure-the contact takes place and an external reaction force is exerted on the nodes involved in the contact. The contact constraint is enforced by the definition of the 'master' surfaces and 'slave' surfaces: only the master surface can penetrate into slave surface and the contact direction is always taken as being normal to the master surface. The indenter surface is chosen as the master surface due to the large stiffness of the indenter with respect to the specimen. The interface between the indenter and the specimen is assumed to be frictionless, since friction has a negligible effect on the nanoindentation process (Edlinger et al., 1993).

The imposed geometrical boundary conditions are: the nodes along the axis of symmetry can move only along such an axis, i.e., the y axis, and all the nodes on the bottom of the mesh are fixed, i.e., the displacement along x and y direction, are constrained.

Because very small indentations are being simulated, the mesh near the indenter is very fine so that it can describe the deformation and stress gradients associated with indentation with sufficient accuracy. And the mesh becomes progressively coarser at distances further away from the indenter. For the mesh shown in Figure 34, area 1 has a mesh size 2nm*4nm, area 2 has a mesh size 10nm*20nm while area 3 has a mesh size of 50nm*100nm. Axisymmetric four node elements are used for the continuum. A zoom-in view of area 1 and part of area 2 are shown below in Figure 35.

To simulate a typical indentation process, a downward displacement is imposed on the indenter; this causes the indenter to push into the surface of the material. Subsequently, the indenter is given an upward displacement until it is free of contact with the specimen. For a given indenter displacement, the corresponding load determination is achieved by summing the reaction forces on the bottom nodes. The load (P)-displacement (h) curve can be plotted and compared to the experimental loading-unloading curve.

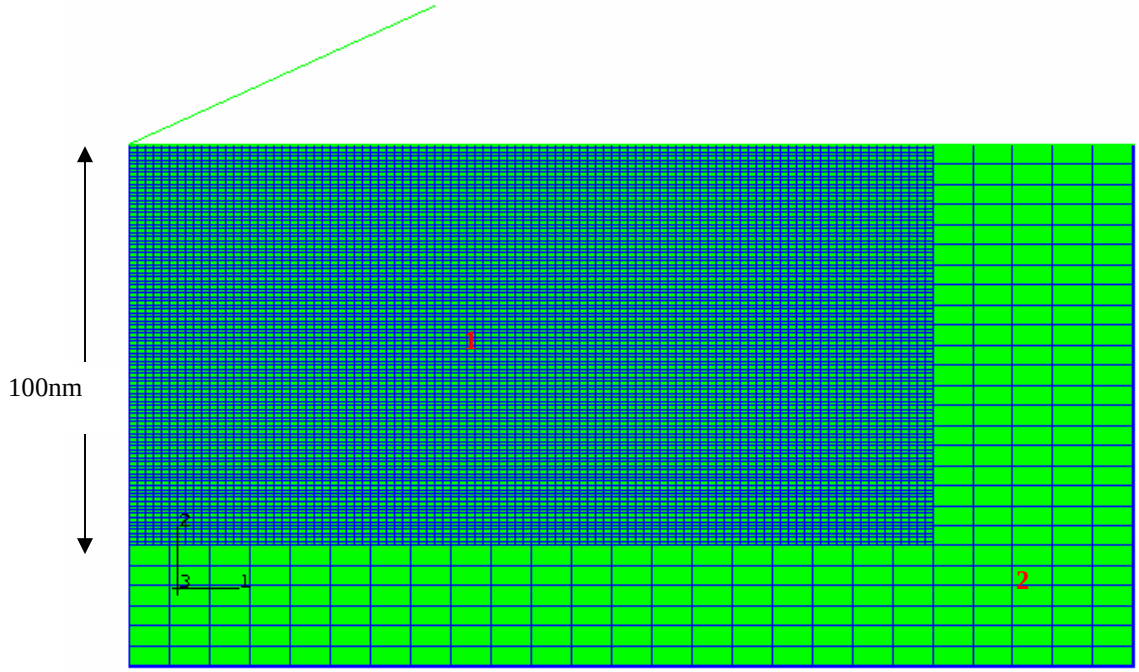

Figure 35: Zoom-in view of fine meshes under the indenter (area I has 2,500 elements)

To verify the current FEM model, the comparison with published experimental results of Pethica el al. (1983) in Bhattacharya and Nix's Paper (Figure 4, 1988) is first repeated here. For this simulation, the material properties of silicon are set to be: Young's modulus, 207 GPa, yield strength, 4,410 MPa, and Poisson's ratio, 0.278 (Bhattacharya and Nix, 1988). Figure 36 shows the comparison of the present FEM analysis and those from Pethica et al. (1983) on indentation of silicon. Since the current FEM results agree well with the experimental work as the FEM work of Bhattacharya and Nix, it can be concluded that the FEM work here is correct.

Note that the FEM model is independent of scale, as the original work was an indentation as large as 300 nm deep, the model presented here is rescaled. The only disadvantage at rescaling is that it will lose some resolution as the minimum mesh size under the indenter is now bigger. For this simulation, a perfect Berkovich tip is used, and as it will be pointed out in the next section, to simulate a shallow nanoindentation, the radius of curvature on the top of the tip must also be considered.

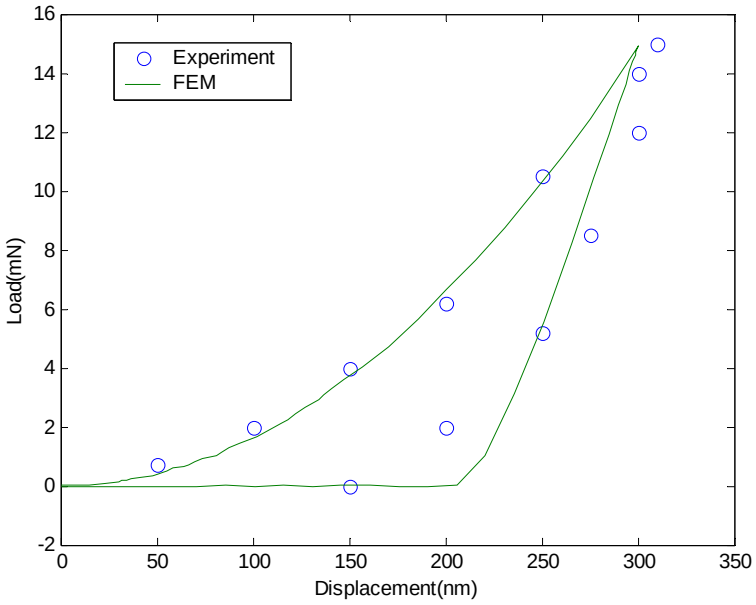

Figure 36: Comparison between the results from the present FEM analysis and those from Pethica el al. (1983) on indentation of silicon

4.3 Tip Radius Calibration

The ideal tip area function is defined as $A = C_0 \cdot h_c^2$, ($A = f(h_c)$), where C_0 is a fixed constant depending on the geometry of the tip. For a Berkovich tip, C_0 = 24.5, and for a 90 degree cube corner tip C_0 = 2.598. To find an equivalent cone for the axisymmetric finite element model, the area at each depth of the conical tip must be the same as the original pyramid tip. Thus, it could be easily seen that

$$\pi(h_c \tan\theta)^2 = C_0 h_c^2 \qquad (10)$$

Where h_c is the contact depth, and θ is the semivertical angle (see Figure 37). For an ideal Berkovich tip, θ = 70.3°, and for an ideal 90 degree cube corner tip, θ = 42.3°. θ = 70.3° is used for the FEM simulation shown in Figure 36.

Because of blunting of the tip and also due to machining differences during manufacturing of the tip, there is always a certain finite radius of curvature on the top of the tip. When the indentation depth is small, most of the contact happens in the uppermost spherical depth range, and the real contact area is quite different from the ideal tip. Therefore, when one performs the nanoindentation experiments, the area function needs to be calibrated for a specific range. Correspondingly, in the nanoindentation FEM, the equivalent tip radius needs to be 'calibrated' to obtain an accurate and simple geometrical representation of the indenter.

4.3.1 90 Degree Cube Corner Tip

To estimate the tip radius for a 90 degree cube corner tip, a method very similar to a standard tip calibration is used. Such method has been briefly described in section 2.1. This method was first proposed by Hysitron, and is improved in this work. Figure 37 below shows a sphere intersecting a plane.

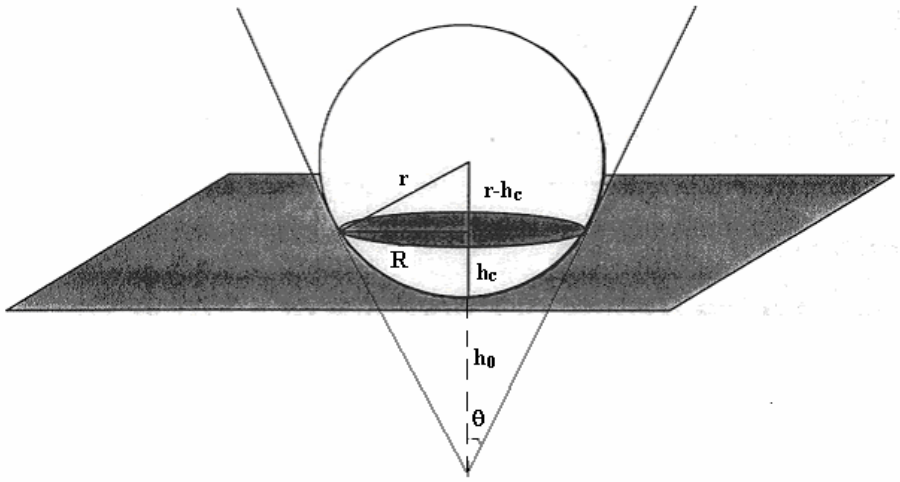

Figure 37: Projected area of sphere

Referring to Figure 37, the projected area of the sphere at a depth "h_c" is represented by the shaded area. The projected area is given by the equation:

$$A_c = \pi R^2 \tag{11}$$

Using the Pythagorean theorem, the radius of the area is also given by:

$$R^2 = r^2 - (r - h_c)^2 \tag{12}$$

Solving Eq. (12) and substituting R into Eq. (11) yields the following function for projected area vs. depth:

$$A_c = \pi h_c (2r - h_c) \tag{13}$$

To determine the area function, a series of indentations must be carried using a standard "calibration" sample, such as fused quartz. The contact area of these indentations is found using the standard modulus equation:

$$A_c = \frac{\pi \left(dP / dh \right)_{unload}^2}{4E_r^2} \tag{14}$$

where P is the indenter load, h_c is the penetration depth, $(dP/dh)_{unload}$ is the experimentally measured stiffness of the upper portion of the unloading curve. The contact area is then plotted versus the contact depth. Using a curve fitting routine, the experimental data is then fit to Eq. (13).

For a typical indenter, the contact area is only in the spherical regime for a short time before the contact area is on the pyramidal area of the tip. Thus, one must carefully choose the data for the fitting. In this work, due to the limitation of data points in the spherical part and inaccuracy in shallow indentations, a combined spherical and conical curve is fitted to the data. The area function is described as

$$\begin{aligned} A_{spherical} &= \pi\, h_c (2r - h_c) \\ A_{conical} &= C_0 * (h_c + h_0)^2 \end{aligned} \tag{15}$$

where h_0 is the distance between the real top of the tip and the apex point of the equivalent conical tip as shown in Figure 37, and could be calculated by

$$h_0 = \frac{r}{\sin\theta} - r \tag{16}$$

The change from $A_{spherical}$ to $A_{conical}$ occurs at

$$h_c = r - r\sin\theta \tag{17}$$

Figure 38 below shows the comparison of several different area functions. It could be seen that the ideal tip $A = C_0 \cdot h_c^2$ doesn't agree with the experimental nanoindentation data points in the range of interest, i.e., 0-40nm; both the area function calibrated in the experiments and the spherical-conical curve discussed in this section fit the data well. As discussed in Chapter 2, the standard area function calibration used in the Triboscope is a very complex function of h_c, which is extremely difficult to represent in FEM by a simple geometry. Thus, the spherical-conical equivalent tip is used in the FEM. For the curve shown in Figure 38, a least square fit was performed and r was found to be 46.91 nm, which agrees with the common tip radius claimed by the producer (http://www.Hysitron.com) of these tips. According to Eq. (17), the depth of the spherical part, h_c is 15.34 nm, which means that the contact of the first 15 nm indentation happens with the spherical part.

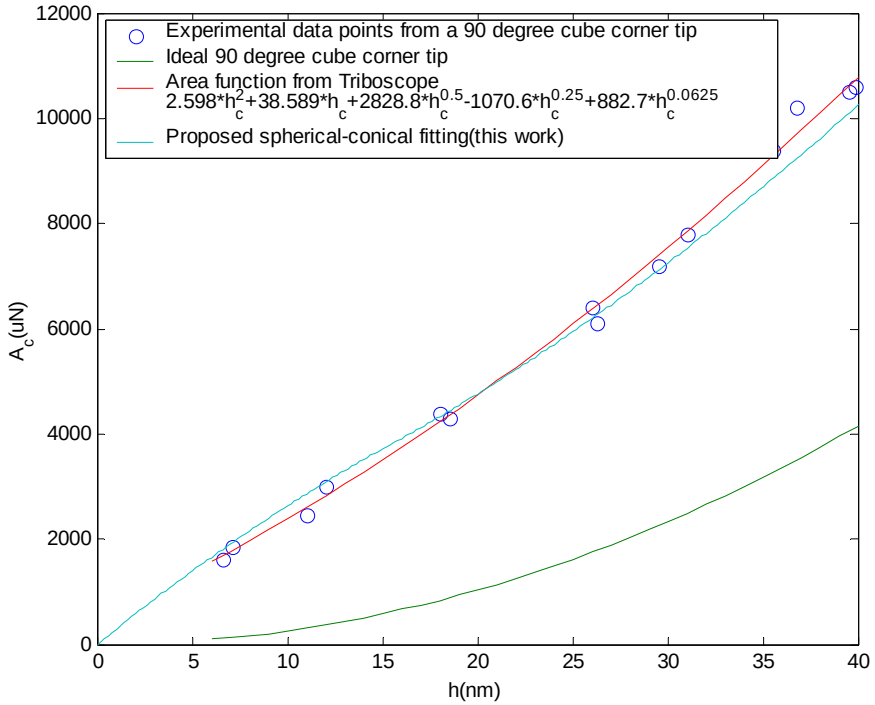

Figure 38: Different area functions for 90 degree cube corner tip

4.3.2 Berkovich Tip

For the Berkovich tip, the spherical radius of the tip is normally around 100 nm to 200 nm, and the semivertical angle, θ = 70.3°. Assuming the tip radius is the average of the two, i.e., 150 nm, according to Eq. (17), the depth of the spherical part, h is only 8.78 nm. Therefore it is very hard to estimate the tip radius by the method above as the spherical part is too small.

To estimate the Berkovich tip radius, the FEM model introduced previously is used. For a sample whose material property is known, the only variable in the simulation is the radius of the tip curvature. Thus, by varying the radius, the simulated loading-unloading curve will change. The best fit with the experimental data will give us the tip radius of the tip.

The fused quartz sample is used as the standard sample for the FEM calibration. The material property is found first by fitting the curve of the cube corner tip indentation, for which the tip radius is a known value for us. Then, the material property is used in the Berkovich tip FEM, and the best radius found is r = 200 nm. The details of the simulation are discussed in the next section.

4.4 Homogeneous Materials

4.4.1 Fused Quartz

Fused quartz is first studied to verify the FEM model mentioned above. From nanoindentation experiments discussed in section 2.4.1, we get an average reduced modulus, E_r=69.6GPa. For the FEM, since we consider the diamond indenter as a rigid body, then

$$\frac{1}{E_r} = 0 + \frac{1-0.17^2}{E_f} \Rightarrow E_f = 67.6GPa$$

E_f is the Young's modulus value that needs to be used for the specimen in the FEM simulations.

One of the nanoindentation loading-unloading curves shown in Figure 9 of Chapter 2 for fused quartz is chosen for comparing. As we could see in Figure 9, the loading-unloading curves of fused quartz are very consistent, thus any of them could be chosen as the one to be compared with the FEM results. Considering the resolution and capability of the FEM model shown above, a 105 μN nanoindentation with a maximum depth of 45.6 nm is used. A series of FEM simulations for 90 degree cube corner tip of 45.6 nm with different yield strengths are done, and the one giving the best fit to the experimental curve is thought to be the yield strength of fused quartz.

Figure 39 shows the best fit of the FEM simulation to the experimental data, and the yield strength is found to be 4.3 GPa. Figure 40 shows a contour of von Mises stress after withdrawal the indenter. Note that the picture is a zoom-in of the view of the model corresponding to Figure 35. The indenter is also shown in the image.

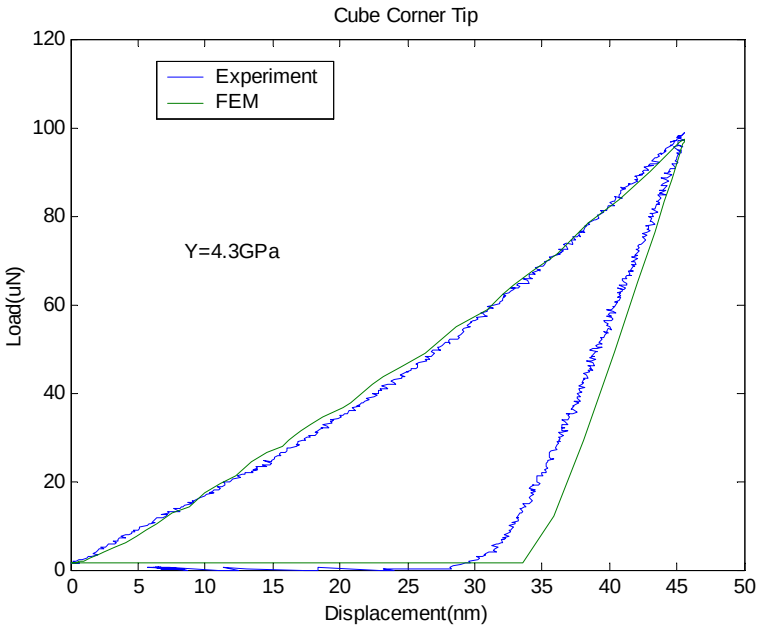

Figure 39: Comparison of FEM and experimental data for cube corner indentation on fused quartz, E = 72 GPa

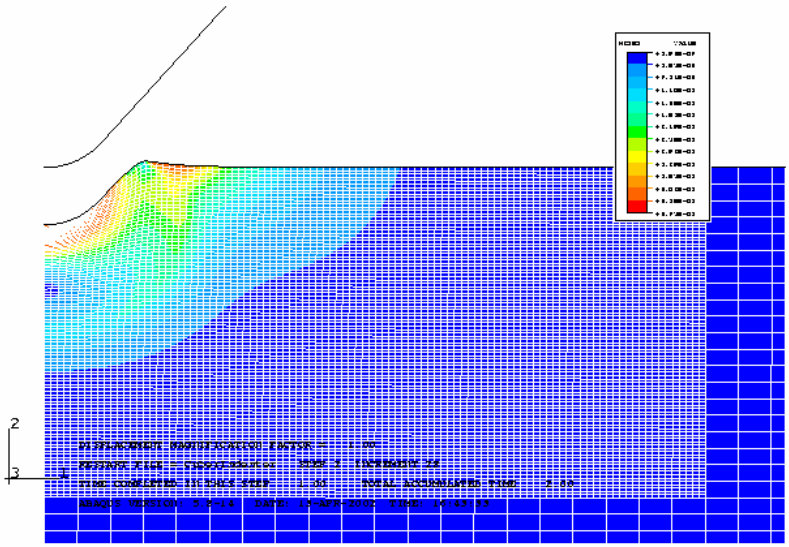

Figure 40: von Mises stress after nanoindentation for a cube corner indentation on fused quartz

Once the yield strength is found, it is then used in a series of nanoindentation FEM simulations to find the radius of the Berkovich tip using the approach described in the previous section. In this work, a 1,500 μN nanoindentation experiment with a maximum depth of 100.07 nm is selected.

Figure 41 shows the best fit of the FEM simulation to the experimental data, from which, the radius of the Berkovich tip is found to be 200 nm. Although the FEM "fitting" is attempted on both the loading and unloading curves, however, there is always some mismatch for materials that undergo large elastic recovery in the unloading process as seen in Figure 41. A detailed discussion will be presented in the next section.

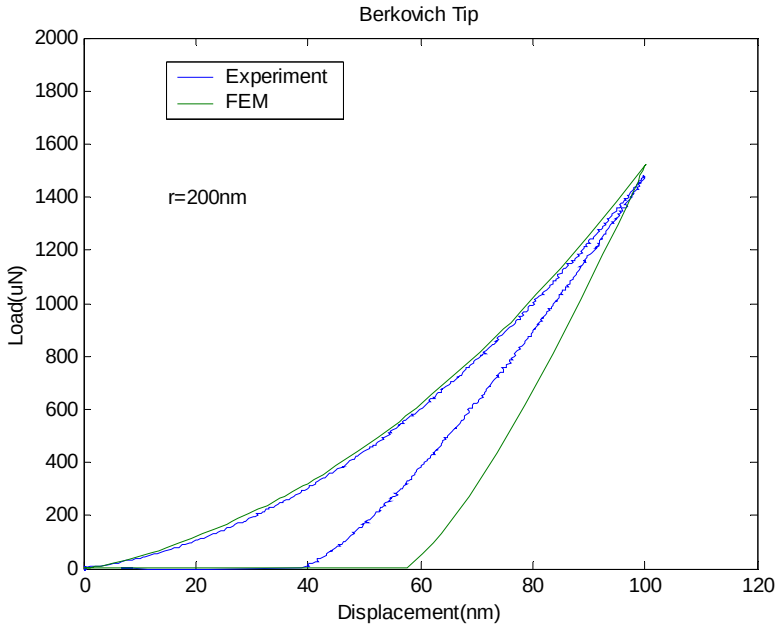

Figure 41: Comparison of FEM and experimental data for Berkovich indentation on fused quartz, E = 72 GPa

Figure 42 shows a contour of von Mises stress after withdrawal of the Berkovich tip. By comparing Figure 42 with the previous Figure 40 for 90 degree cube corner tip, it could be easily seen that the 90 degree cube corner

tip is much sharper than Berkovich tip. Also, the shapes of the von Mises stress contours are quite different due to the difference in indenter geometry.

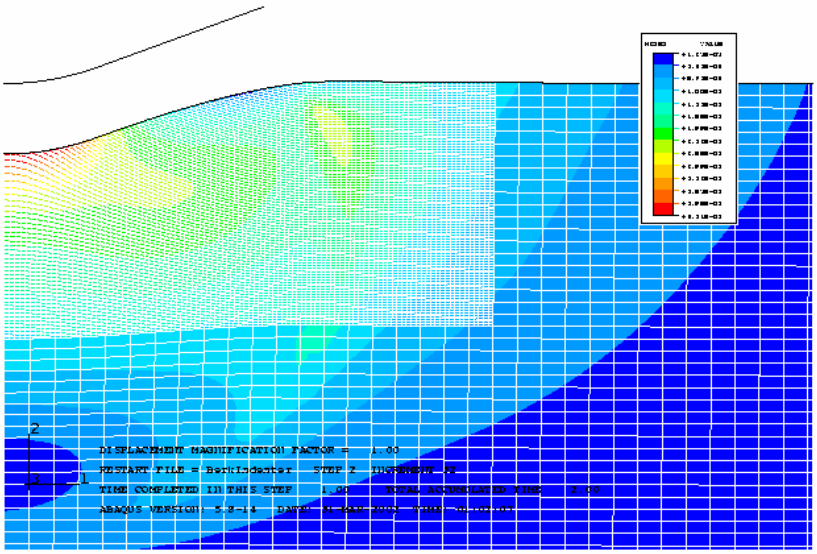

Figure 42: von Mises stress after nanoindentation for a Berkovich indentation on fused quartz

4.4.2 Silicon

From the experiments on silicon described in Chapter 2, one can obtain the Young's modulus and hardness for each loading-unloading curve. Note again that the curves and the material properties are very consistent for all the depths except the known 5 nm layer of silicon oxide on top of the surface. From the experiments, the average reduced Young's modulus is found to be 165.6 GPa. Therefore, in the FEM simulation, since we consider the diamond indenter as a rigid body,

$$\frac{1}{E_r} = 0 + \frac{1-0.278^2}{E_f} \Rightarrow E_f = 152.8GPa$$

E_f is the Young's modulus to be used in the FEM simulation for the silicon specimen. Also note that the tip radius established in the previous section are used in these simulations.

Figure 43 shows the best fitting when varying the yield strength. The yield strength for the best fit is found to be 4.2 GPa. The nanoindentation experimental data used here is one curve in Figure 12 of Chapter 2 (100 μN nanoindentation with a maximum depth of 36.4 nm).

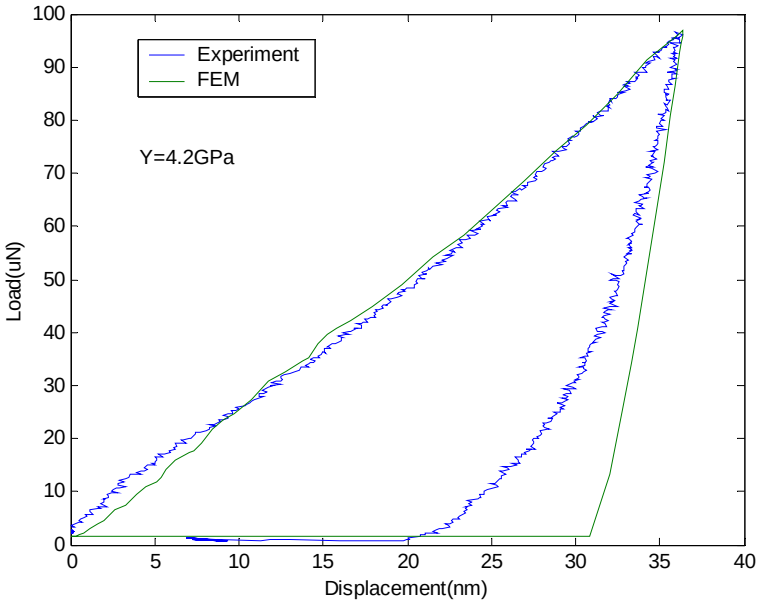

Figure 43: Comparison of FEM and experimental data for cube corner indentation on silicon

When we use the material properties from the cube corner fitting, and the radius of curvature from the previous section, the FEM simulation result and comparison with the experiment using the Berkovich tip are shown in Figure. 44. A 2,800 μN nanoindentation with a maximum depth of 103.8 nm is selected as the experimental data to be compared. Note that this is really a confirmation (no fitting) for the values obtained above. It could be seen that there is some discrepancy between the experimental data and the FEM simulation. Comparing Figure 39 and Figure 41, or Figure 43 and Figure 44, it is seen that there is bigger mismatch in the FEM fitting for Berkovich nanoindentation, especially the unloading part. This may be due to the inexact material model used; elastic-perfect plastic behavior is only an approximation and not an exact description of the material we are dealing with. It seems that the larger the plastic deformation, the better is the approximation. Therefore, we see better fitting for cube corner nanoindentation, since the plastic deformation is relatively large. Also, for a brittle material like silicon, it really does not have a well-defined yield strength, but instead has a fracture strength about 7GPa (ASM Handbook, 1990). Also, due to the silicon oxide layer that is present on the surface, the cube corner fit may give a lower yield strength than the real silicon value. Thus, when this lower value is used for the Berkovich tip, the loading-unloading curve is somewhat lower than expected (see Figure 44).

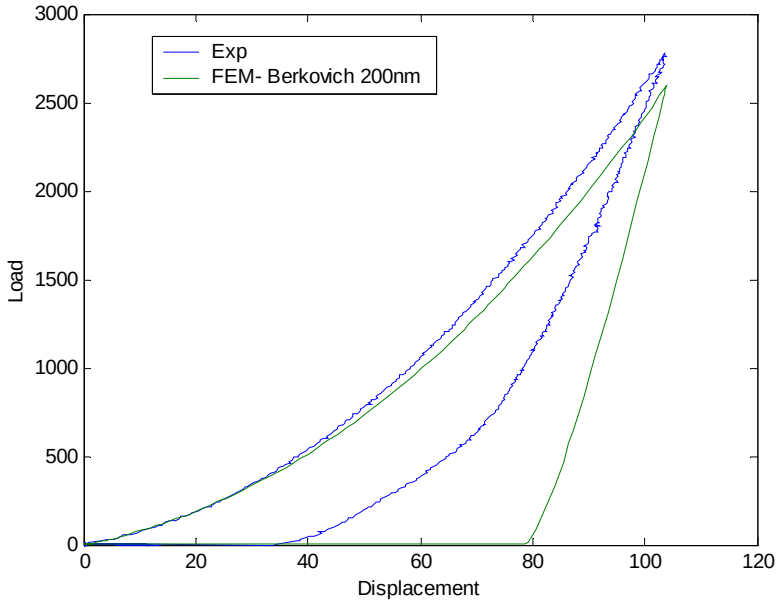

Figure 44: Comparison of FEM and experimental data for Berkovich indentation on silicon (E = 178.6 GPa, Y = 4.2 GPa)

4.5 Deposited Thin Film: 100 nm Gold Thin Film on Silicon

Next, we will employ the FEM modeling to the deposited thin film that has been discussed in section 2.5. From previous FEM studies, the detailed geometries of the 90 degree cube corner and the Berkovich tips are already known. As pointed out in section 2.5, the adhesion layer does not have a significant effect on the nanoindentation behavior of the material, therefore, the 2 nm adhesion layer is neglected in the FEM modeling.

For this study, the silicon material property is still taken as the value from the FEM fitting for cube corner nanoindentation, i.e., E_{Si} = 178.6 GPa and yield strength, Y_{Si} = 4.2 GPa. These material properties give good agreement when the penetration of the indentation is small in both Figs. 43 and 44. As we will see below for the deposited thin film, the indentations are mainly happened in the top 100 nm gold film, and only the top of the silicon substrate gets involved.

Examining the experimental data, three indentations at approximately 12 nm depth are thought to be representative of the deposited gold properties (based on indentations of 10 – 20% of the overall film thickness). It was found from the experiments that the average reduced Young's modulus for the gold coating is 99.2 GPa. Therefore, for the FEM, since we consider the diamond indenter as a rigid body

$$\frac{1}{E_r} = 0 + \frac{1-0.42^2}{E_f} \Rightarrow E_f = 81.7GPa$$

E_f is the Young's modulus we should use for the gold layer in the FEM simulation.

In the FEM model, all parameters are known except the yield strength of the 100 nm gold film. Through curve fitting of the load-displacement data, it is found the yield strength of the gold film to be approximately 800 MPa as shown in Figure 45. Even though this value is higher than the published bulk gold value (tensile strength = 127 MPa, ASM Handbook, 1990), one must consider that this is a deposited thin film material property, and may greatly differ from that of the bulk material.

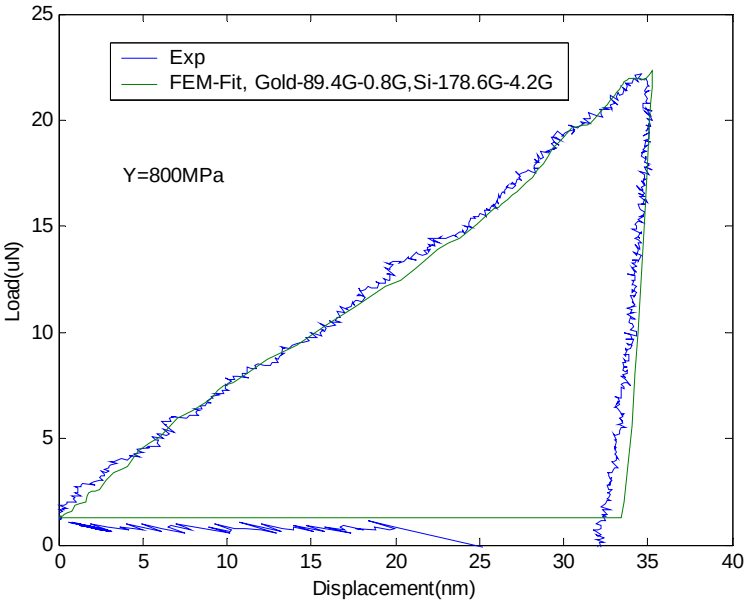

Figure 45: Comparison of FEM and experimental data for cube corner indentation on 100 nm Au on Si sample

Once the thin film yield strength is obtained (from low depth indentation curve fitting), this yield strength (800 MPa in this case) is used in an FEM model of a deeper indentation on the same surface. Ideally, this indent will have combined properties of both the thin film layer and the substrate material, thus by comparing the FEM simulation to the experimental load-displacement data, the film yield strength can be verified if a match is obtained. Figure 46 below shows the results of a 100 nm deep indentation and corresponding FEM model results. Note there is no fitting process in Figure 46, the good agreement proves the correctness of tip radius and the material properties obtained before.

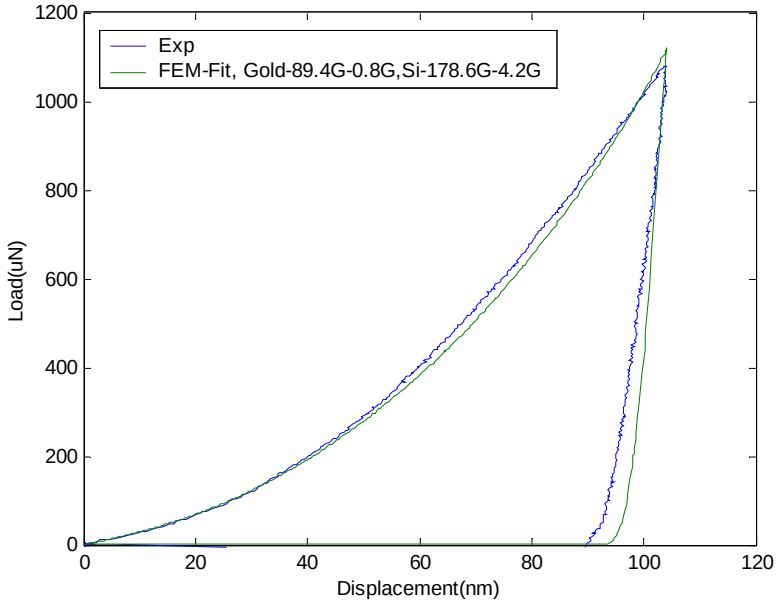

Figure 46: Comparison of FEM and experimental data for Berkovich indentation on 100 nm Au on Si sample

Figure 47 below illustrates a contour of von Mises stress plot of the indentation performed to a maximum depth of 35 nm, corresponding to the experimental data in Figure 45. This shows that the subsurface residual stresses extend to approximately 130 nm below the surface, which is much greater than that of the maximum depth of the indent. Figure 47 shows a larger pile-up than previous Figure 40 for 90 degree cube corner indentation on pure silicon, which agrees with the experimental observation that large pile-up exists for indentation on soft film-hard substrate materials pair.

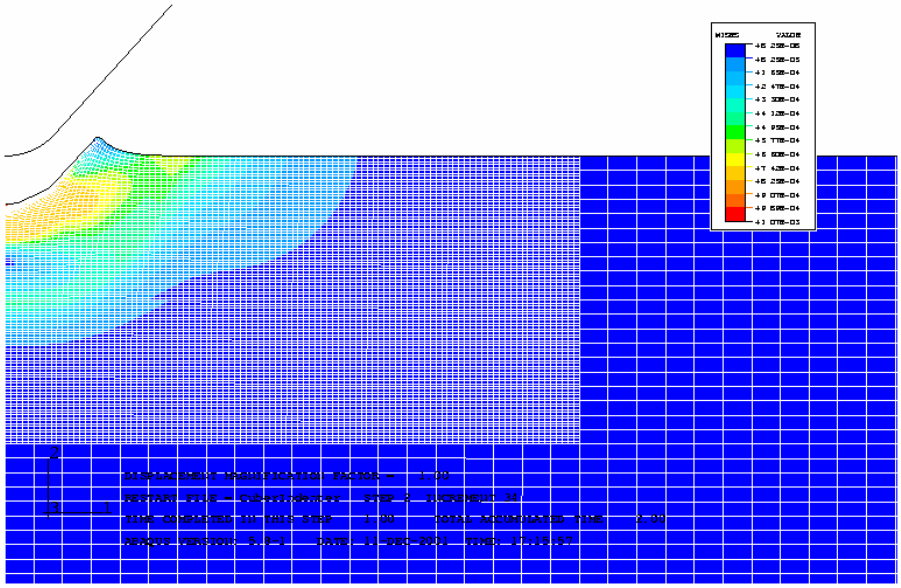

Figure 47: von Mises stress after cube corner nanoindentation on 100 nm Au on Si sample

4.6 Engineering Al390-T6 Sample

As discussed in Chapter 2, engineering surfaces (e.g., Al390-T6 sample) are much more complex than the homogeneous and deposited thin film surfaces discussed until now in three aspects. First, samples like Al390-T6 have a roughness around 200-300nm, compared to the typical indentation depths that vary from 10 to 200nm. Second, engineering samples have unknown layer thickness, and third, even for each layer, there are random distribution of various material particles, such as Si and Cu (layers are not homogeneous). However, for further modeling and investigation of the scuffing failure mechanism of Al390-T6 sample, an approximate layered structure needs to be generalized. Previous work by Patel (2001) and Pergande (2001) pointed out that the top 50 nm layer of such sample have obvious different chemical compositions and mechanical properties than the substrate below.

In this work, an iterative method is proposed and used to extract the material properties for the top layer and the substrate.

4.6.1 Proposed Iterative Method

If we have an indentation deep enough compared to the surface layer, then the loading-unloading curve should be mostly determined by the substrate material. Thus, we could first find the substrate material properties from the FEM fitting for deep indentations by assuming that the material is homogeneous. Once we find that, we can use this as a base, and perform FEM fitting for shallow indentions to find the material properties for the layer on the substrate (assume two layers material, substrate is counted as a layer).

In principle, this method could also be used iteratively for multilayered materials. The material properties from bottom to the top may be found by sequentially fitting different indentation results. Theoretically, one could find the material properties for any number of layers.

Also, once we find the material properties for the top layer, we can then substitute back into the fitting for the bottom layer, and try to improve the fitting there and get a more accurate yield strength for the bottom layer, and then repeat.

4.6.2 Application of this method

For the Al390-T6 sample, we assume there is a 50 nm layer on the substrate. As we saw in Figs. 20, 21 in Chapter 2, the loading-unloading curves are not very consistent due to the various reasons discussed before. Thus, to best represent the average material behavior, a median experiment is chosen for both Figs. 20 and 21. These are a 60 μN 90 degree cube corner nanoindentation with a maximum depth of 44.56 nm and a 2,500 μN Berkovich nanoindentation with a maximum depth of 192.13 nm.

Recall form Figure 22 in Chapter 2 that the reduced Young's modulus from the experiments was very consistent through all the depths. The average E_r for the top 50 nm nanoindentation is 88.5 GPa, while average E_r for the substrate below being 88 GPa. Thus, the value should be used in the FEM model is

$$\frac{1}{E_r} = 0 + \frac{1-0.33^2}{E_f} \Rightarrow \begin{cases} E_{f-top50nm} = 78.9GPa \\ E_{f-sunstrate} = 78.4GPa \end{cases}$$

Figure 48 shows the best fitting when we take the material as a homogeneous one and fitting for a deep Berkovich indentation to find the material property of the substrate. The yield strength of the substrate is found to be 1,100 MPa.

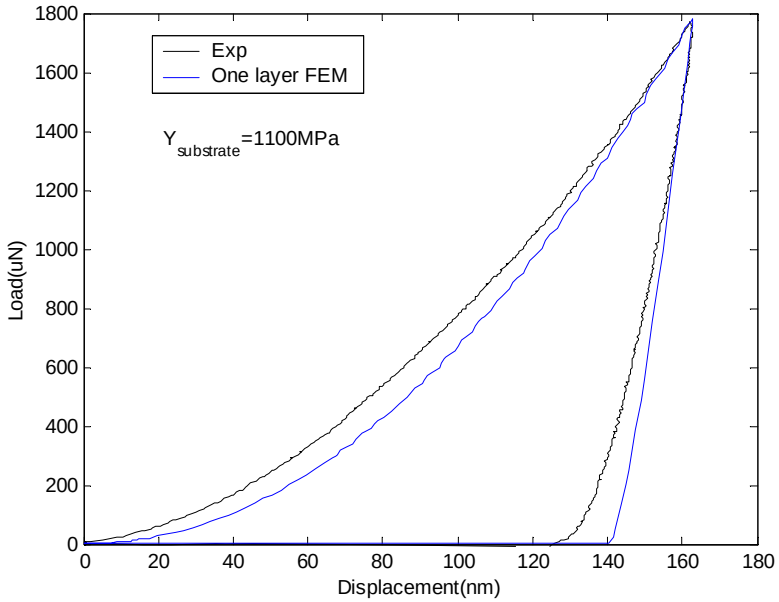

Figure 48: Comparison of FEM and experimental data for Berkovich indentation on engineering Al390-T6 sample

As expected, the middle part of the FEM loading curve is lower than the experimental one, as there is actually a top layer on the sample, whose yield strength should be higher as the hardness value is higher.

Using the previous material properties as the substrate material properties, and FEM fitting for a cube corner nanoindentation curve is then carried out. Figure 49 shows the best fitting, which gives us a yield strength of the top 50 nm layer of 1,800 MPa.

Having obtained the properties for both layers, the simulation for the Berkovich indentation is repeated, using the two layer model. Such an improved model results in the curves shown in Figure 50.

Theoretically, one can still improve the accuracy of the representation of the sample by using the iterative method discussed in the previous section. There are two reasons for us to stop here. First, not much information about layers within the top 50 nm is available, and second, the current two-layer FEM model gives a good agreement to the experimental results as seen in Figs. 49 and 50.

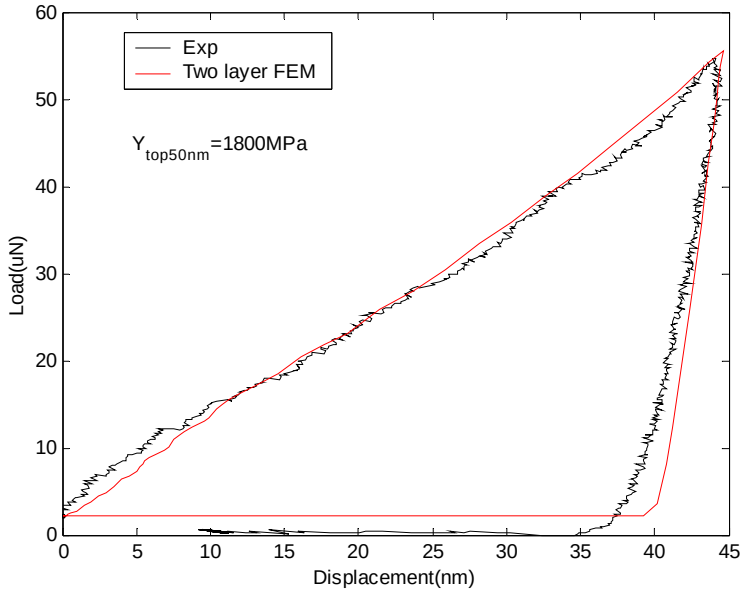

Figure 49: Comparison of FEM and experimental data for 90 degree cube corner indentation on engineering Al390-T6 sample

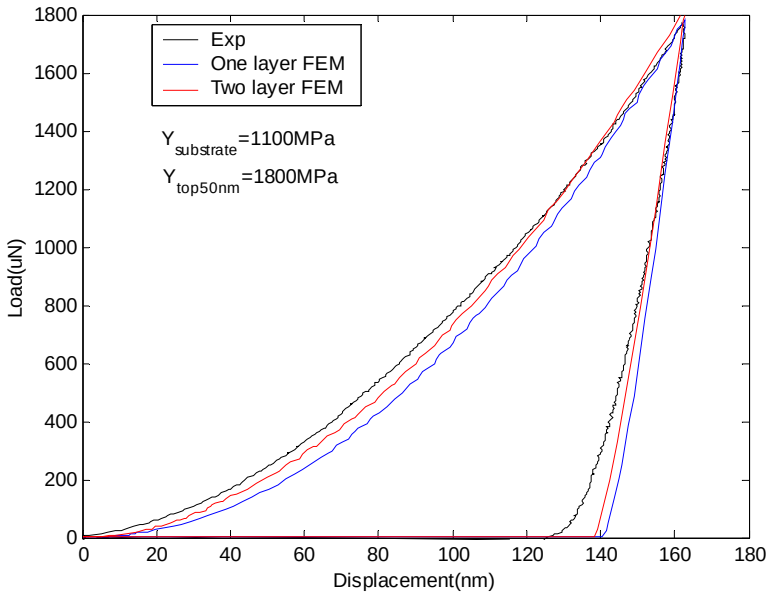

Figure 50: Comparison of FEM and experimental data for Berkovich indentation on engineering Al390-T6 sample

4.7 Summary

A Finite Element model is built to simulate the nanoindentation experiments and obtain additional information about the material layers and their properties. A combined experimental and FEM method is proposed and used to find the exact geometry of the tip for FEM analysis. The aforementioned nanoindentation experiments on homogeneous, deposited thin film, and unknown Al390-T6 surfaces are simulated, and a very good agreement between FEM simulation and the experimental loading-unloading curves is found. By using the FEM analysis, the yield strength of the different surface layers could be obtained. It is also found that FEM could help identify the material properties for very thin films or layered materials where separately nanoindentation experiments alone are unable to distinguish the properties of each layer. For the engineering rough Al390-T6 sample, a robust iterative method is proposed and successfully implemented to find the material properties from the substrate to the top layers.

Chapter 5. Thermomechanical FEM Analysis for Shoe-Disk Sliding Contact in High Pressure Tribometer

5.1 Background

As discussed in the Introduction, the main objective of the overall project is to investigate the scuffing mechanism. Tribological testing was performed using the High Pressure Tribometer (HPT) as discussed in Chapter 1. A schematic of the HPT is shown below in Figure 51.

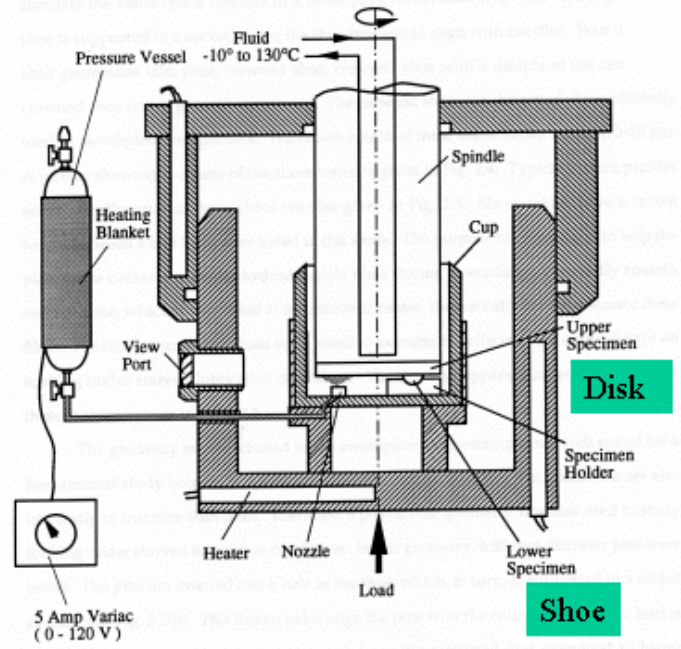

Figure 51: Shoe-disk sliding contact in High Pressure Tribometer (e.g., Patel, 2001)

A widely accepted scuffing hypothesis is related to the contact temperature that scuffing occurs when a critical surface temperature is reached, thus lowering the shear strength of the material interface (e.g., Blok, 1937). The contact surface temperature model used in most engineering application of dry and boundary lubricated sliding has been the classical model of Blok (1937 and 1963) which considers the contact surface temperature problem as a semi-infinite body subject to a single concentrated heat source. Rashid and Seireg (1987) used the finite difference method to study the transient temperatures in concentrated contacts with a lubricant film. Several studies have examined elastic-plastic sliding contact. However, analytical solutions of elastic-plastic contact require many simplifying assumptions in order to obtain a tractable problem (Merwin and Johnson, 1963; Jiang and Sehitoglu, 1994).

As a result of the complexity associated with analytical approaches to the thermomechanical problem, the analysis of thermomechanical sliding contact has remained mostly within the domain of finite element methods. Serpe et al. (1998) performed a thermomechanical analysis of sliding rings using a 2-D axisymmetric finite element model. Ye and Komvopoulos (2001) studied the sliding contact between the slider and disk in a hard disk drive using a 3D finite element model.

In the current study, a thermomechanical FEM analysis will be performed for the shoe-disk sliding contact that occurs in the HPT. From the study in the previous chapters, we established that the Al390-T6 is relatively rough, with a 50 nm major harder layer on the top. The contact is under a starved lubricated condition, and the effect of lubricant is also considered.

5.2 Macro-Modeling

5.2.1 Model

Obviously, the sliding contact in the HPT is a coupled thermal mechanical problem. Normally, the thermomechanical FEM problem is relatively complex, and takes an extreme large memory and CPU time to solve. Therefore, the problem needs to be first reasonably simplified. A macro-model is first considered, in which the Al390-T6 surface is treated as an infinitely smooth and homogeneous surface.

From (Patel, 2001), we know that the total scuffing duration under the prescribed condition (see Figure 2 in Chapter 1) is about constant for the samples tested. Therefore, scuffing always occurs at a normal load of about 500 1bs, i.e., 2,224 N. In this FEM study, the scuffing process is thought to be history-independent, thus 2,224 N is thought to be the constant load.

Details of the contact geometry are shown in Figure 52. Furthermore, by studying the wear marks on the steel shoes after tribological testing (see Figure 53), it is found that only part of the shoe area is in contact with the disk during the sliding.

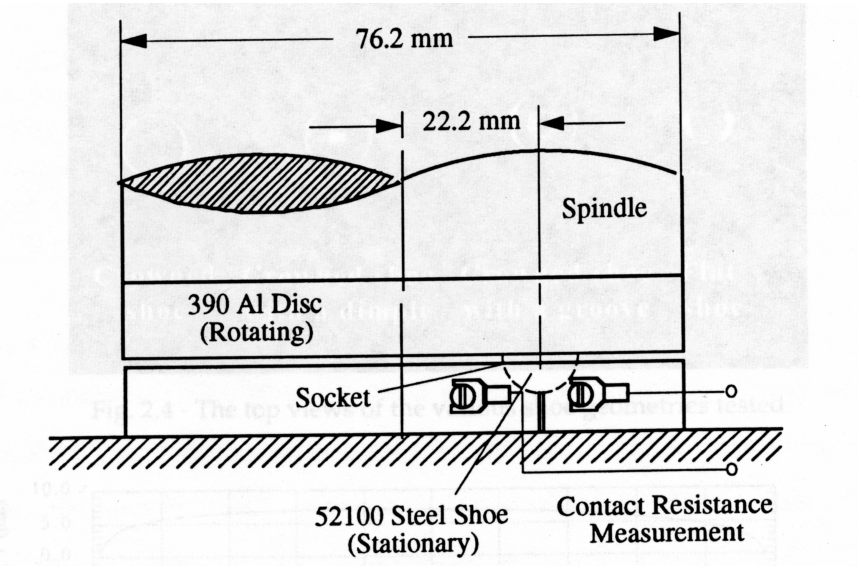

Figure 52: Contact geometry between disk and shoe (from Patel, 2001)

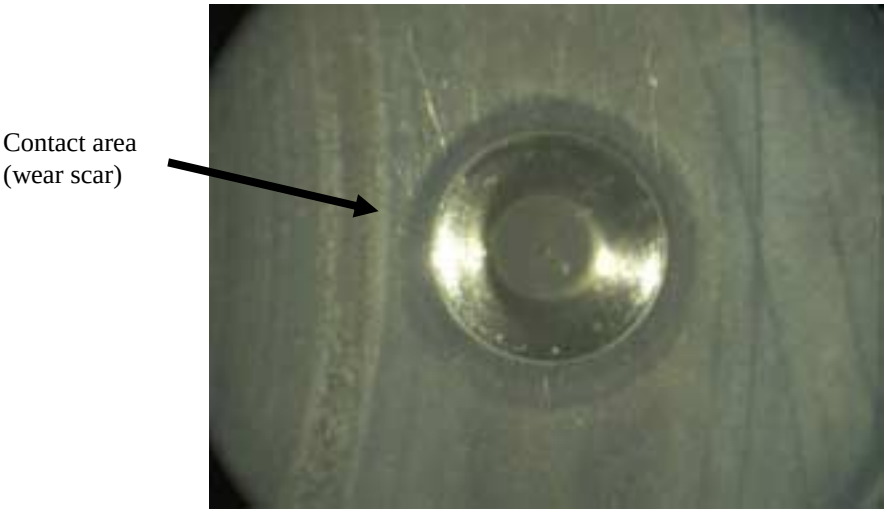

Figure 53: Wear marks on the steel shoe

This is due to the fact that the steel shoes are crowned in nature with a large dimple as shown in Figure 54. It could be seen in Figure 53 that only the inner side of the crowns (relatively to the center of the disk) is in severe contact. It can be explained that in the Stribeck Curve, for the range of starved lubrication contact, the friction coefficient increase when the linear speed decrease, therefore, the inner part has a higher friction coefficient, and thus a higher wear rate.

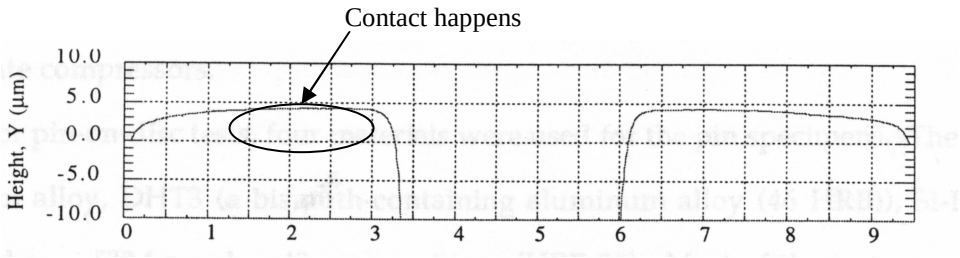

Figure 54: Typical surface profile of crowned shoe with dimple

Based on the shoe geometry, an equivalent rectangular area with dimensions 6mm×1mm is used in the FEM modeling. Similarly, to reduce the complexity of the problem, only a ring part of the disk is used in the FEM model. The model is shown in Figure 55.

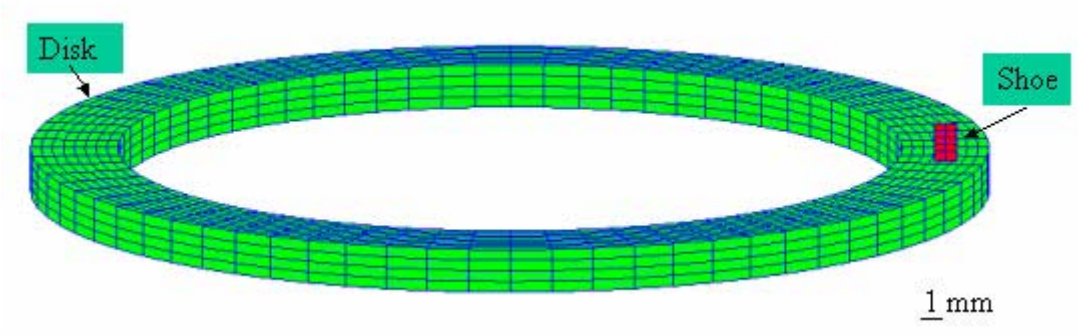

Figure 55: FEM macro-model

The effect of lubrication is taken into consideration by the convection coefficient, *h*. The exact value for *h* is usually unknown and one needs to perform careful experiments to obtain the *h* value for a specific application. It is hard to get an accurate *h* value without careful experiment. Typical values are h = 40 w/(m^{2}K) for a rotating disk in air and h = 900 w/(m^{2}K) for a rotating disk in water. For this work, h = 100 w/(m^{2}K) is thought to be reasonable, and used for the following simulations.

The roughness effect is first neglected in the macro-modeling, and it is later realized that the roughness may be the key effect in the scuffing mechanism as discussed in the next section.

In the current model, the material is assumed to be homogeneous, and bulk material properties of the Al390-T6 disk found in Chapter 4, Young's modulus, E = 84.9 GPa, and yield strength, Y = 1,100 MPa are used. The steel shoe is considered to be rigid as it is much harder and stiffer than the Al390-T6 disk.

The initial and environment temperature is set to be 120 °C.

5.2.2 Results

Figure 56 below shows the contour of von Mises stress after one rotation. Note that the maximum von Mises stress is only 73.8 MPa, much lower than the yield strength. It implies that the load itself is relatively small to

cause failure, there must be some thermal effect, to either reduce the strength of the disk by increasing the temperature or local melting that causes the scuffing.

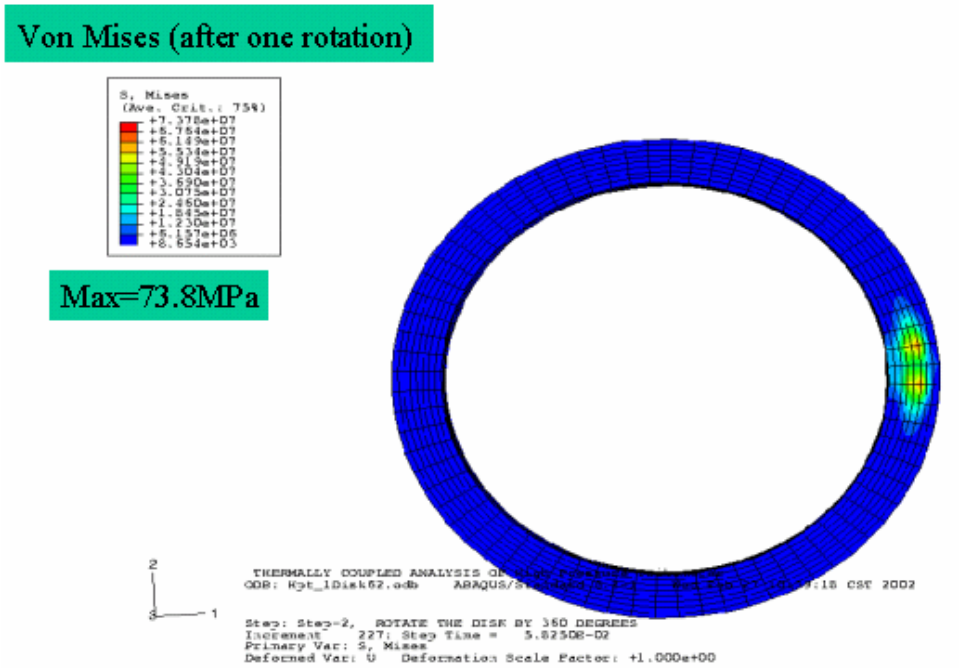

Figure 56: Contour of von Mises after one rotation

Figures 57 and 58 show the contours of temperature for the disk after one rotation and two rotations, respectively. Note that the maximum temperature increase is only 0.4°C. Also there is no obvious temperature accumulation after each rotation.

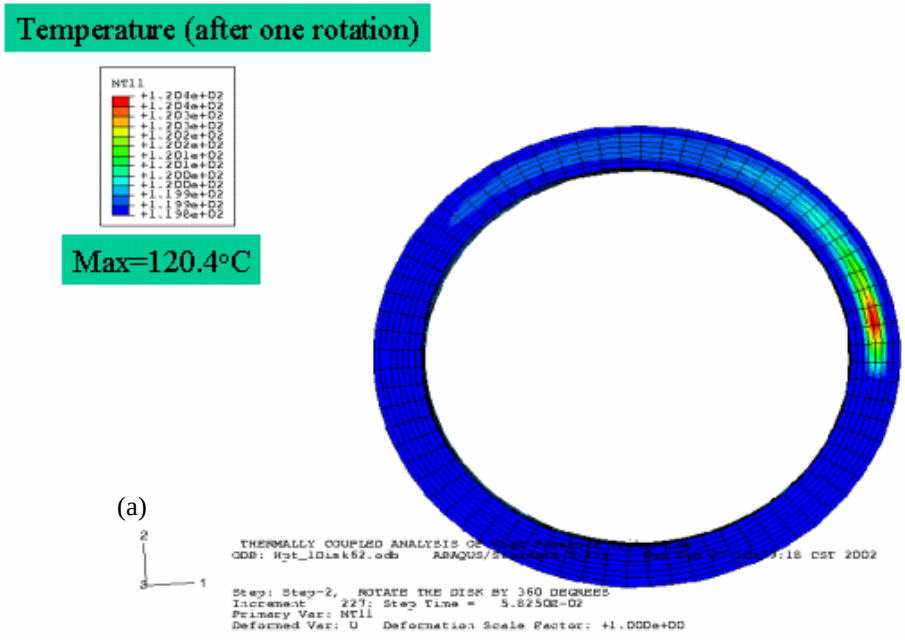

Figure 57: Contour of temperature after one rotation

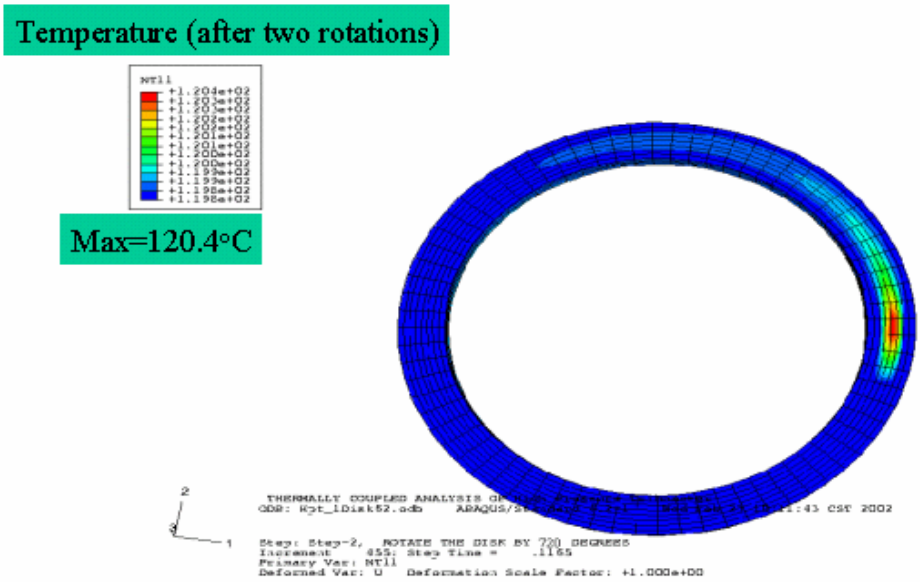

Figure 58: Contour of temperature after two rotations

As we see from the above results, the macro-modeling does not give much information about the cause of scuffing as there is no significant bulk material temperature increase observed. This agrees with the phenomena observed by Cavatorta and Cusano (2000) when they performed the pin-disk starved lubricated contact in the HPT. Also, other researcher's FEM works reach the same conclusion (e.g., Serpe et al. 1998).

5.3 Micro-Modeling

5.3.1 Introduction

The real engineering surfaces always have certain roughness. When the Al390-T6 disk and 52100 steel shoe are loaded together in High Pressure Tribometer, it is the asperities of the surfaces that must first carry the applied load, and the real contact area is much smaller than the nominal area used before. Thus, the local contact stress and temperature increase could be extremely high, which is termed Flash Temperature by Blok (1937). The previous macro-model cannot represent the contact happen in the asperity level. Also, since the dimension of that model is in the order of centimeters, it is extremely hard to model the nm thicker layer found in previous Chapters due to the complexity of the thermomechanical problem. Therefore, a micro-model (asperity contact) model is proposed as described below.

- Al390-T6 disk surface is modeled by a collection of spherical asperities with certain statistical distribution and the steel shoe is thought to be a smooth surface since $Rq_{Al}/Rq_{steel}>=10$.
- Contact at an asperity with height of 3σ, where most severe contact occurs, will lead to surface failure. σ is the standard deviation of asperity heights, which could be found from roughness measurements. Therefore, the Greenwood and Williams (1966) statistical model could be used to find the separation d when certain normal load is exerted. A schematic is shown in Figure 59.

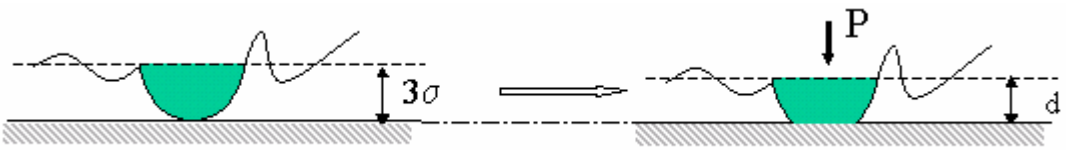

Figure 59: Asperity contact

Once we obtain *d*, an asperity model like the one shown in Figure 60 will be used. The asperity will first move downwards by a distance of 3σ-d, then slide horizontally a certain distance.

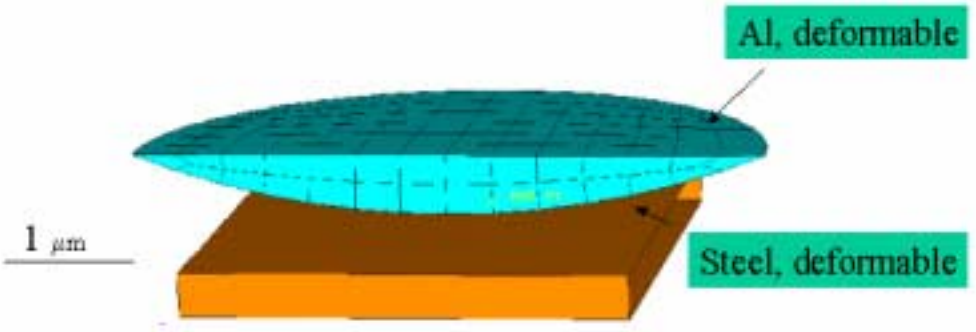

Figure 60: FEM micro-model

5.3.2 Statistical Analysis

As reported in Patel (2000), the 52100 steel shoe used for the HPT experiments has an average Rq of 0.03 μm, which is less than 1/10 of the Rq value of its contact pair Al390-T6 Disk. Therefore, the steel shoe is thought to be smooth, and the roughness parameters of Al Disk as shown in Table 4 is used in the statistical calculation.

Table 4: Roughness measurement of Al disk

	Rq (mm)	R (mm)	$\eta(mm^{-2})$	skewness
Surface	0.2	8	0.03	-0.2

In the current model, the material is assumed to be homogeneous, and bulk material properties of the Al390-T6 disk found in Chapter 4, Young's modulus, E = 84.9 GPa, H = 3 GPa, and yield strength, Y = 1,100 MPa are used. The steel shoe is considered to be rigid in this statistical analysis as it is much harder and stiffer than the Al390-T6 disk.

As described before, the critical load at scuffing failure is found to be 2224N (500 lbs). And the nominal contact equivalent area is a rectangle of 6mm*1mm.

A weibull distribution described in Yu and Polycarpou (2001) is used for the statistical analysis here since the Al-disk as shown in Table 4 has a skewness of –0.2. The standard deviation of asperity heights σ is found to be 0.183 μm using Equation 7 in Yu and Polycarpou (2001).

The mean separation vs. external normal load for this contact pair is plotted in Figure 61. From Figure61, the mean separation under the critical load is found to be 0.187 μm.

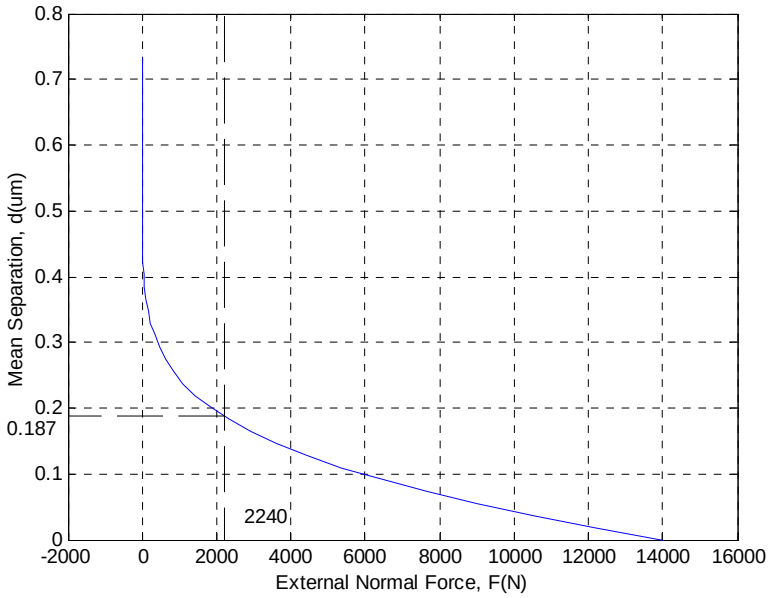

Figure 61: Mean separation under critical load

Also, the real contact area is found to be only 1.74% of the nominal contact area, see Figure 62. It explains to some extent why the contact stress is relatively low and there is no obvious temperature accumulation observed in the macro-model, in which a nominal area is used.

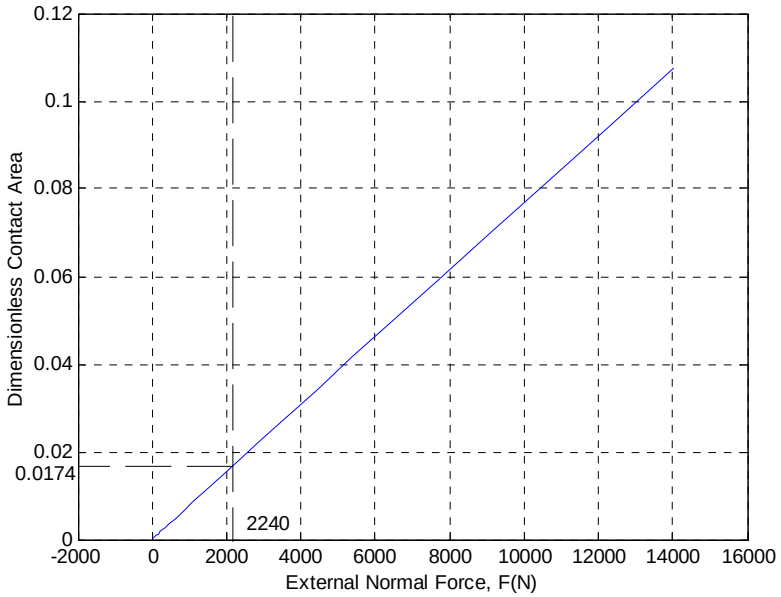

Figure 62: Real contact area under critical load

Therefore, in this micro-model, an Al asperity with the height of 0.55 μm will first be moved towards the steel show surface by 0.364 μm.

5.3.3 Finite Element Analysis

5.3.3.1 Geometry and model

The Al asperity is thought to be spherical, the height of the asperity is only 0.55 μm while the approach distance of the asperity is 0.364 μm, both are very small compared to the radius of the asperity, 8 μm as shown in

Table 4. Therefore, a cap like geometry is used to represent the asperity, as shown in Figure 60. The steel shoe is modeled by a plate as it is much smooth and large compared to an asperity. The width of the plate is currently set to be 6 μm, slightly larger than the diameter of the top surface of the asperity; the length of the plate is set to be 6200 mm, approximately the length of the scuffing marks in the relatively slide direction, and the height of the plate is currently set to be 800 μm. The dimensions used here is not strictly correct, further study could be done to find better dimensions to model this problem more correctly and efficiently.

The Al asperity and steel plate are modeled with C3D8T elements. Frictional contact between the asperity and the plate is modeled by contact pairs between surfaces defined on the element faces in the contact region. The mesh is shown in Figure 63. This mesh is rather very coarse with only are two elements through the thickness of the asperity, fifteen elements along the diameter of the top circular surface of the asperity and three elements through the thickness of the plates. There are altogether 555 nodes and 336 elements for the asperity, and 176 nodes and 63 elements for the plate.

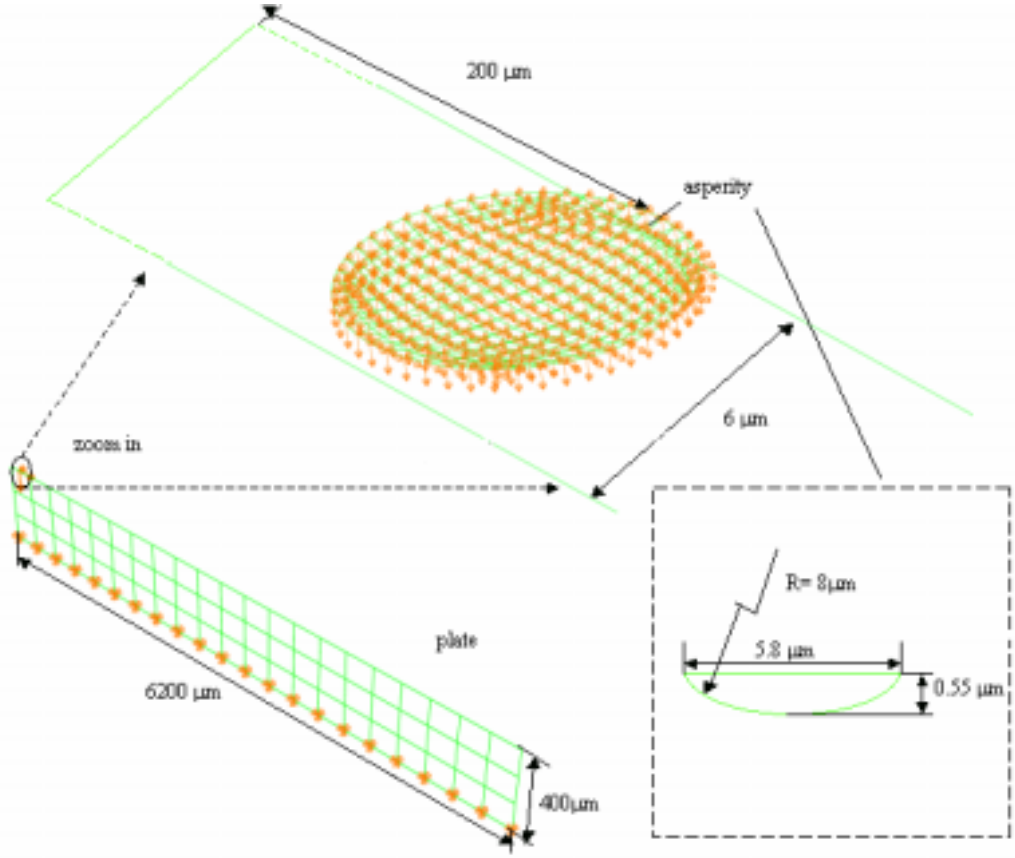

Figure 63: Mesh of the model

5.3.3.2 Material properties

The material properties are taken from the previous nanoindentation results and ASME handbook as listed in Table 5. The friction coefficient is set to be 0.2 for the current modeling, a very common value for solid-solid contact. It is assumed that all the frictional energy is dissipated as heat and the default distribution is used. The *GAP HEAT GENENRATION options allows the user to specify an unequal distribution. The gap conductance is first chosen to be 10^{-9}, a slightly high value from the example 4.2.19 of the abaqus handbook for disk-brake contact.

Table 5: Material properties used in FEM simulations

	Al-390 T6	52100 Steel
Young's modulus, E (GPa)	84.9	205
Yield strength, Y (GPa)	1.1	2.0
Poisson's ratio, ν	0.33	0.3
Thermal expansions, (μm/m·°C)	18 @ 20°C 22.5@ 250°C	11
Density, ρ (kg/m^3)	2730	7800
Specific heat, c (J/kg·°C)	963	452
Conductivity, k (W/m·°C)	134	48

5.3.3.3 Loading and boundary conditions

The asperity is first pressed against the plate by using an applied boundary condition to set the top surface of the asperity move downward by 0.364 μm linearly in a very short time. Here in the current simulations this short time period is set to be 10^{-8} seconds. After that, the asperity is moved horizontally in x direction by 6000 μm by using another applied boundary condition, and the motion is linearly with time and finished in 2.5e-3 thus the speed of the relative motion is 2.4 m/s as in the previous macro-model.

The other degrees of freedoms for the top surface of the asperity are fixed during these two steps, and so do all the degrees of freedom for the bottom surface of the plate. All the boundaries are first set to be adiabatic. Later, some different boundary conditions are studied.

The initial temperature of the model is set to be 120°C.

5.3.3.4 Results and discussion

Three different boundary conditions and sliding distance are studied, and the parameters are listed in Table 6.

Table 6: Different Cases Studied

	Gap heat generation	Gap conductance (J/s·m^2·°C)	Thermal boundary condition	Sink Temperature (°C)	Film Coefficient (J/s·m^2·°C)	Sliding Distance (μm)
Case I	0.5	10^9	Adiabatic	N/A	0	6000
Case II	1	0	Adiabatic	N/A	0	12
Case III	1	0	Top surface of asperity T=120°C	120	100	6000

5.3.3.4.1 Case I

Figure 64 shows the contour of Von mises stress of the asperity at the end of the simulation for Case I. A significant fraction of the asperity body reaches the yielding point, 1100 MPa. Note that in the previous results from macro-model, the maximum Von mises force is only 73.8 MPa, and both the shoe and disk is in elastic deformation. Therefore, the stress in the asperity is much higher than that estimated using a macro-model. Since the plastic deformed fraction of the asperity is surrounded by the elastic deformed fraction as shown in Figure 64, no major plastic flow should happen at this stage.

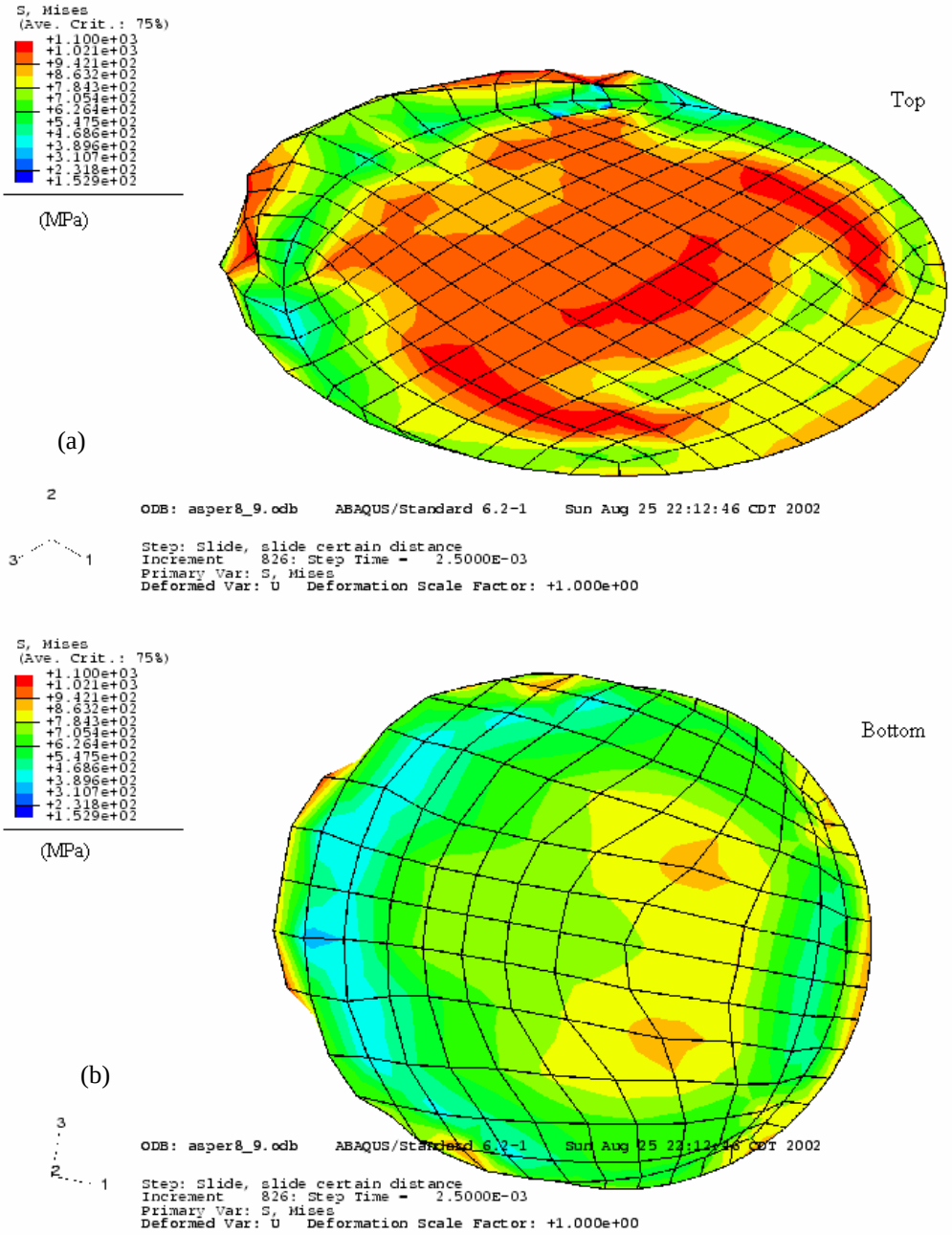

Figure 64: Contour of Von mises stress of the asperity: (a) Top view; (b) Bottom view

Figure 65 shows the temperature contour of the asperity. The temperature increase in this simulation is only 2°C, much less than we would expect. It may due to the fact that a lot of frictional heat entering into the asperity finally is conducted into the plate, as the plate is much bigger than the asperity in this model.

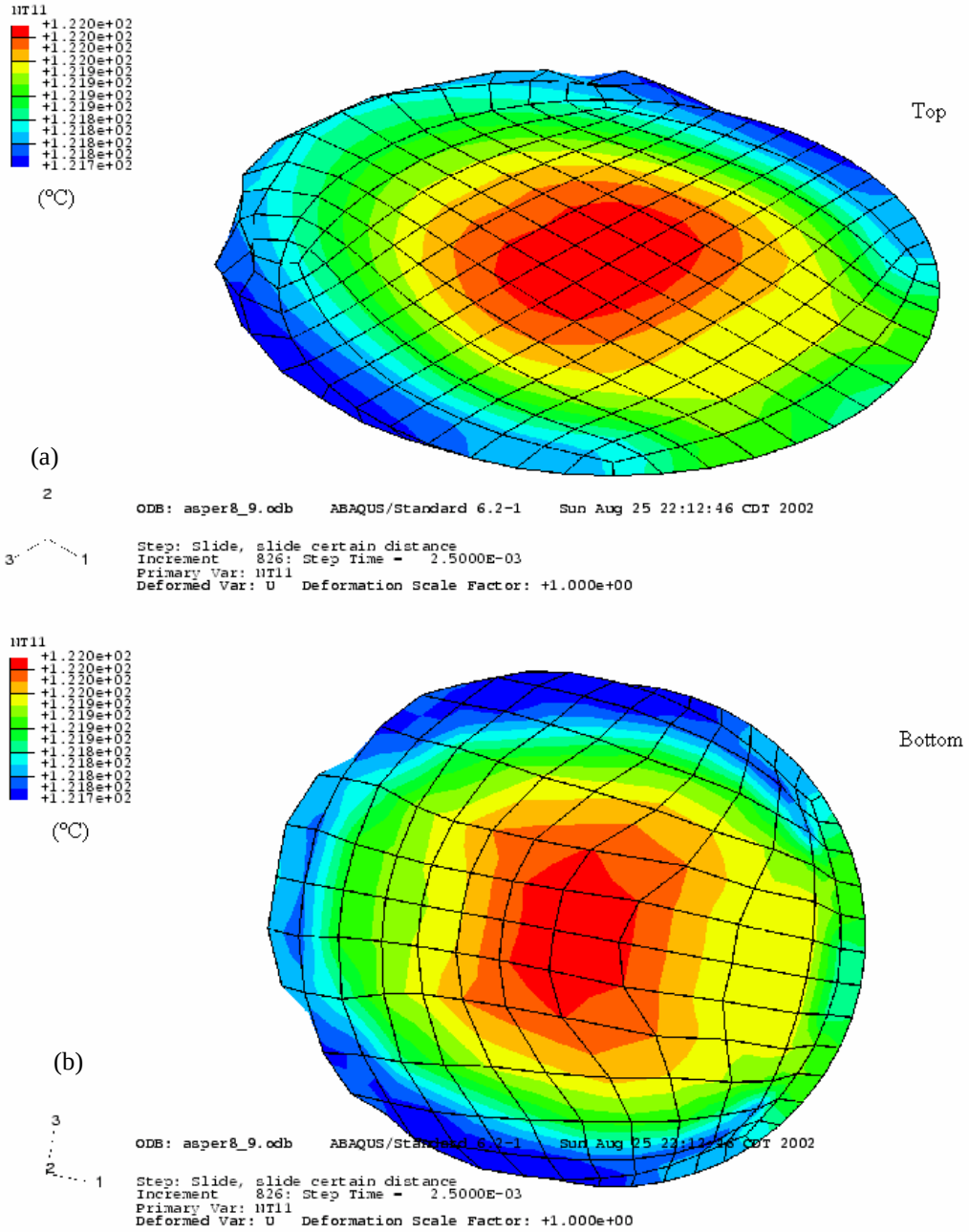

Figure 65: Contour of temperature of the asperity: (a) Top view; (b) Bottom view

Figure 66 shows the history of temperature increase of the bottom node of the asperity. The temperature increases fast at the very beginning and then oscillate around some stable value after $0.2*10^{-3}$ seconds, which is corresponding to a 500 μm sliding.

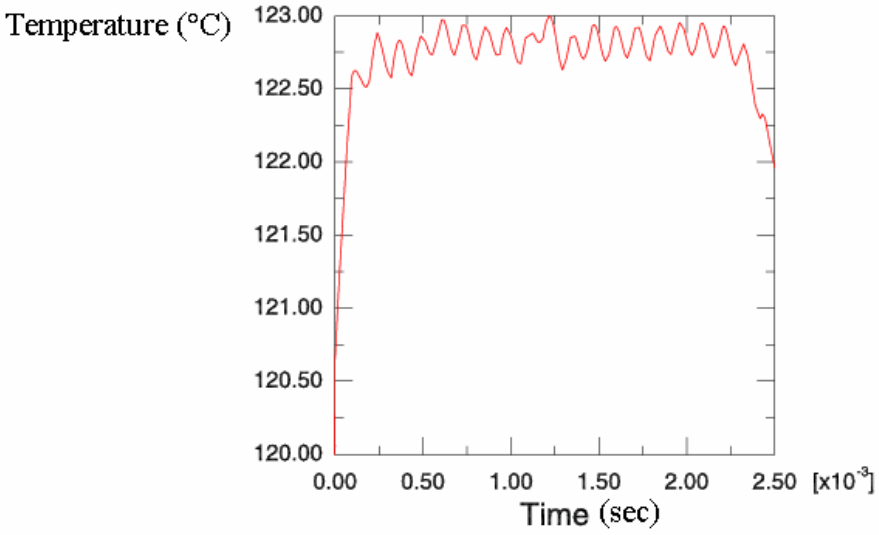

Figure 66: Temperature increase of the bottom node of asperity

Figure 67 shows the displacement of the bottom node of the asperity. Note that the U2 displacement actually reflects the indentation depth of the Al asperity into the steel plate.

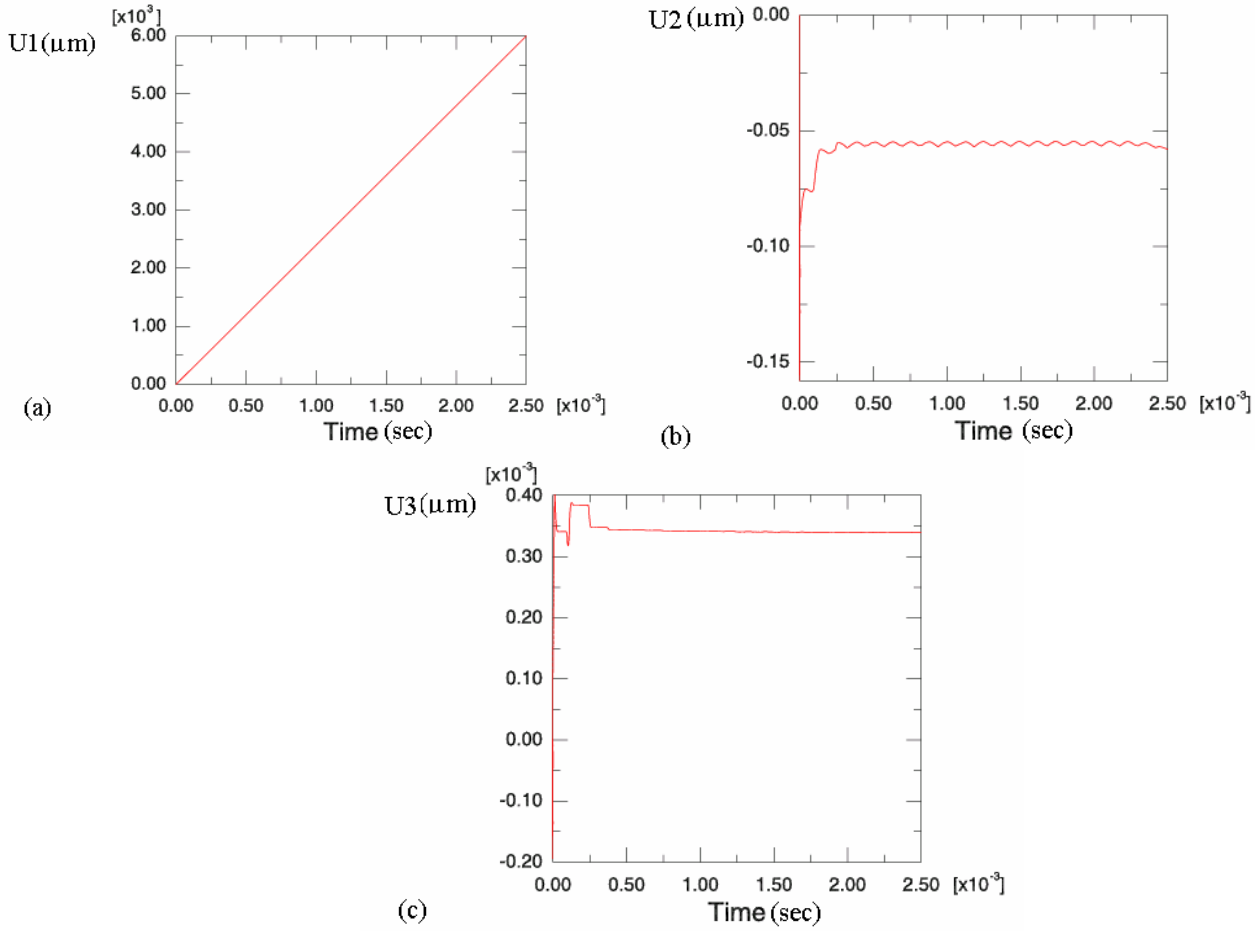

Figure 67: Displacement of the bottom node of the asperity: (a) U1; (b) U2; (c) U3

5.3.3.4.2 Case II

Since there is no significant temperature increase in Case I, and it is thought to be caused by the heat flow from the asperity to the plate, a second case with all the energy inside the asperity is studied. Unfortunately, in this case, with the same boundary condition, the FEM simulation could not converge for the sliding of 6000 μm long. The maximum sliding distance for the case II specified in Table 6 is 12 μm, and the Von missed contour and temperature contour are shown below.

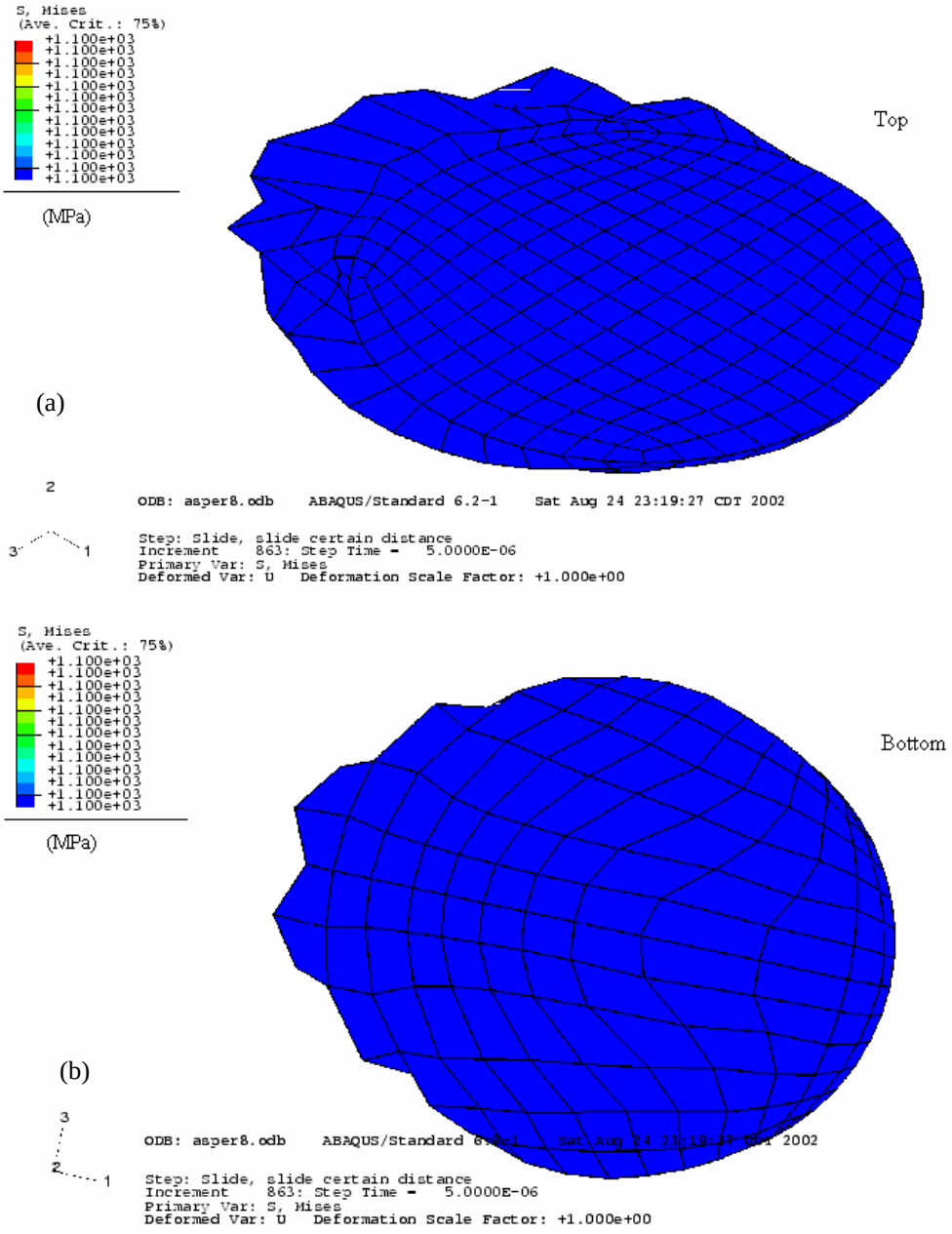

Figure 68: Contour of Von mises stress of the asperity: (a) Top view; (b) Bottom view

Figure 68 shows the Von mises contour, in which the whole asperity gets into plastic deformation. In this condition, a major plastic flow will happen and actually the asperities in the Al disk will flow around, and the so-called scuffing will happen.

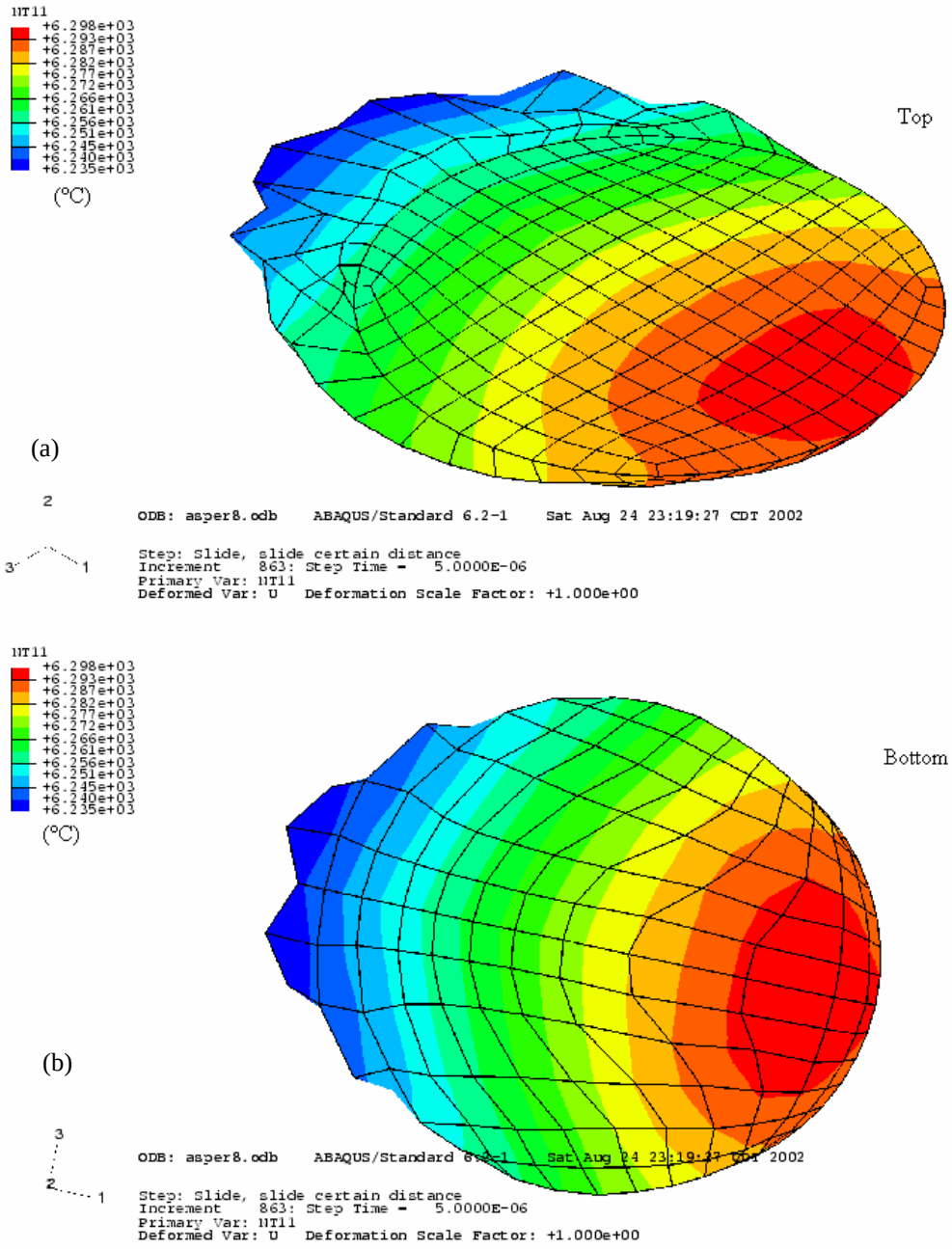

Figure 69: Contour of temperature of the asperity: (a) Top view; (b) Bottom view

The major reason for the difference of the Von mises contour between two cases could be explained from the temperature contour of case II as in Figure 69. As we expected, a temperature increase of 6000 °C is observed in this simulation, which should be the reason of the high stress status of the asperity in this case.

In reality, the increase of 6000°C will not happen, as the asperity will have dramatic plastic deformation or been melted before it reaches such a high temperature. And here, we assume all the frictional heat energy enter into the small asperity and be kept within it, which is really an extreme case. The real condition should between Case I and Case II.

5.3.3.4.3 Case III

Practically speaking, the asperity is not adiabatic as assumed in Case I and Case II. As described before, the temperature is set to be 20 °C at the non-contact side of the disk, which is about 1 centimeter away from the asperity. Also, the air in the chamber will work as a temperature sink. In Case III, a T=120 for the asperity top surface and a film properties for the environment effect is considered. The results are shown in Figure 70 and Figure 71.

Figure 70 shows the Von mises contour, which are similar to the one in Case I.

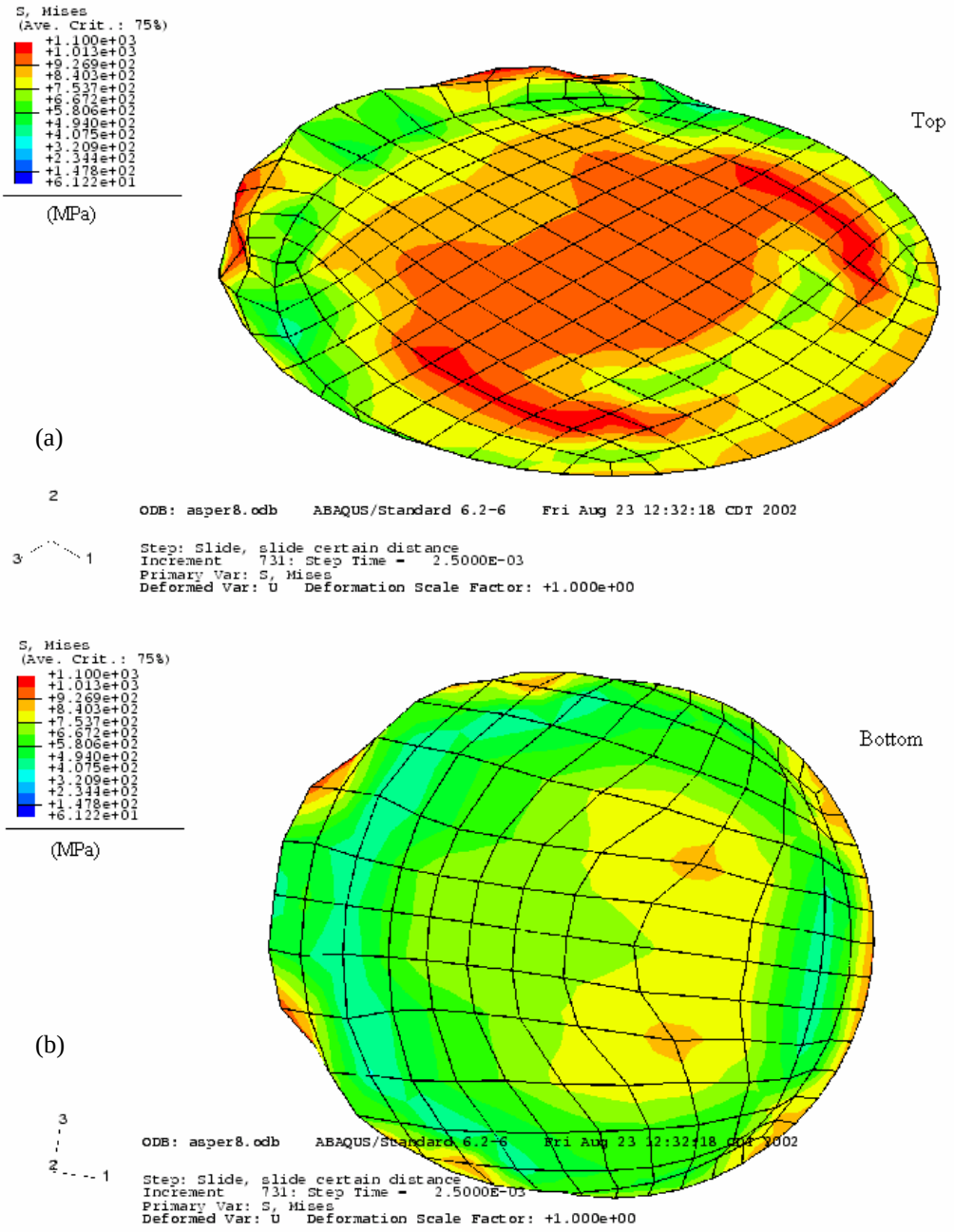

Figure 70: Contour of Von Mises of the asperity: (a) Top view; (b) Bottom view

Figure 71 shows the temperature contour of the asperity. The top view shows the top surface is restricted to have a T=120°C. The bottom view shows the maximum temperature increase is 11°C. As the other parameters are the same as Case II, which has a temperature increase of 6000°C, the increase in temperature here is really small. It is not a surprise as for such a small asperity with boundary condition just several μm away, and the environment working as a sink, the temperature could not be too big as the temperature gradient is a finite number.

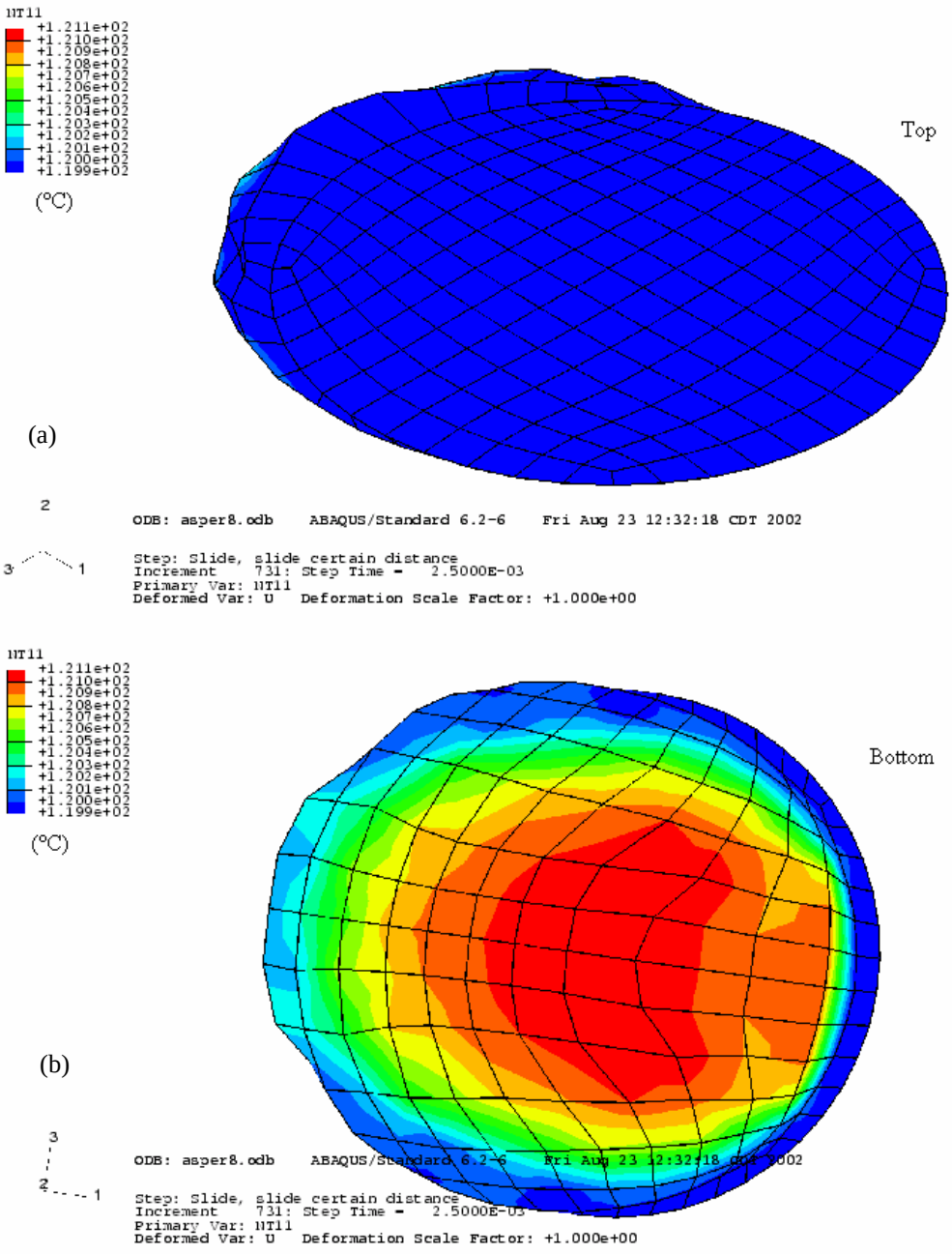

Figure 71: Contour of temperature of the asperity: (a) Top view; (b) Bottom view

5.4 Summary

Thermomechanical FEM analysis for the shoe-disk contact in the HPT is investigated to study the scuffing mechanism. A macro-model is first built and found that there is no obvious cause of surface failure due to stress or temperature. A micro-model is then built and successfully shows that the local contact stress and temperature

increase could be extremely high under the critical loading. Also, it shows that scuffing should be a combination effect of stress and temperature increase.

There are still a lot of parameters need to be further investigated in this model, like the gap conductance, the film coefficient. Also, the range of the asperity considered in the model need to be further studies, since we want to consider one asperity independently but also want to have the correct boundary condition. Further work need to be done to model the nanometers layer in the asperity to see the effect of those thin films.

Chapter 6. Conclusions and Recommendations

6.1 Conclusions

Nanoindentation experiments are performed on different homogeneous, deposited thin film, and engineering rough Al390-T6 surfaces. The results are consistent with the previous study by Pergande (2001). From the study of known deposited thin film (100 nm gold film on silicon), it is found that the hardness value for the multilayer surfaces is not well defined and the value itself is determined by both the top thin film and substrate material properties unless the penetration depth is very large and well into the substrate.

Alternative approaches in studying the nanoindentation experiments have also been tested. It is found that the load, P, vs. the square of penetration depth, h^2, linear relationship works quite well in identifying different layers and their thickness. However, the prediction of the slope of P vs. h^2 still has an error of about 25% and maybe improved by studying other homogeneous materials to obtain more accurate indenter constants. The Johnson's equation that relates the yield strength to measured Young's modulus and hardness is also used and although the results deviate somewhat from later more accurate FEM work, it still seems to be valid for certain materials, such as ductile metals.

A Finite Element model is built to simulate the nanoindentation experiments and obtain additional information about the material layers and their properties. A combined experimental and FEM method is proposed and used to find the exact geometry of the tip for FEM analysis. The aforementioned nanoindentation experiments on homogeneous, deposited thin film, and unknown Al390-T6 surfaces are simulated, and a very good agreement between FEM simulation and the experimental loading-unloading curves is found. By using the FEM analysis, the yield strength of the different surface layers could be also obtained. It is also found that FEM could help identify the material properties for very thin films or layered materials where separately nanoindentation experiments along are unable to distinguish the properties of each layer. For the engineering rough Al390-T6 sample, a robust iterative method is proposed and successfully implemented to find the material properties from the substrate to the top layers.

Thermomechanical FEM analysis for the shoe-disk contact in the HPT is investigated to study the scuffing mechanism. A macro-model is first built and found that there is no obvious cause of surface failure in the stress or temperature. Then, a micro-model is built and successfully shows that the local contact stress and temperature increase could be extremely high under the critical loading. Also, it shows that scuffing should be a combination effect of stress and temperature increase.

6.2 Recommendations

Very useful information has been obtained from the study of the deposited thin film of 100 nm gold on silicon, which is the case of soft thin film on a hard substrate. A further study with known hard thin film on soft substrate is expected to give additional information.

To further examine the validation of Johnson's equation for nanoindentation experiments, more experiments are suggested to be done on ductile materials, such as Al, Cu and Au. This method could be very useful for those materials if it is valid, as it saves time and no FEM analysis will be needed.

The proposed iterative method in the FEM for nanoindentation for unknown layered surfaces is supposed to be very robust. Further application of this method on other multilayer systems is needed to verify this method.

For the thermomechanical FEM analysis of the shoe-disk contact in HPT, a careful experimental study of the convection coefficient will be very helpful to build an accurate model. Further work should be concentrated on the micro-model as it is seen that the asperity contact is likely to be the cause of the scuffing.

References

Abaqus Manual, Hibbitt, Karlson & Sorensen, Inc, 2000.

ASM Materials Handbook, Properties and Selection: Nonferrous Alloys and Special-Purpose Materials, Vol. 2, 10th Edition, 1990

Bhattacharya, A. K. and Nix, W. D., "Finite Element Simulation of Indentation Experiments," *Int. J. Solids Structures,* Vol. 24, No. 9, 1988, pp. 881-891.

Blok, H., "The Theoretical Study of Temperature Rise at Surfaces of Actual Contact under Oiliness Lubricating Condition," *Proc. Inst. of Mechanical Engineering General Discussion of Lubrication,* Vol. 2, 1937, pp. 222-235.

Blok, H., "The Flash Temperature Concept," *Wear,* Vol. 6, 1963, pp. 483-493.

Bonin, W.A., "Capacitive Transducer with Electrostatic Actuation," US Patent No. 5,576,483.

Cavatorta, M. P. and Cusano, C., "Running-in of aluminum/steel contacts under starved lubrication Part I: surface modifications," *Wear,* 242 (2000), pp. 123-132.

Cavatorta, M. P. and Cusano, C., "Running-in of aluminum/steel contacts under starved lubrication Part II: Effects on scuffing," *Wear,* 242 (2000), pp. 133-139.

Doerner, M. F. and Nix, W. D., "A method for interpreting the data from depth-sensing indentation instruments," *J. Mater. Res.*, Vol. 1, No. 4, 1986, pp. 601-609.

Dyson, A., "Scuffing – A Review, Part I," *Tribology International,* 8, 1975, pp. 117-125.

Edlinger, A. K., Gratacos, P., Montmitonnet, P., Felder, E., "Finite element analysis of elastoplastic indentation: Part I - Homogeneous media," *Eur. J. Mech. A/Solids,* Vol. 12, 1993, pp. 679.

Greenwood, J. A. and Williamson, B. P., "Contact of Nominally Flat Surfaces," *Proc. R. Soc. London, Ser A,* 295, 1966, pp. 300-319.

Hainsworth, S. V., Chandler, H.W. and Page, T. F., "Analysis of nanoindentation load-displacement loading curves," *J. Mater. Res.*, Vol. 11, No. 8, Aug 1996, pp. 1987-1995.

Hysitron, Inc., "Tip Calibration Procedure."

Jiang, Y., and Sehitoglu, H., "An Analytical Approach in Elastic-Plastic Stress Analysis of contact," *ASME J. Trib.*, Vol.116, pp. 577-587.

Johnson, K. L., "The Correlation of Indentation Experiments," *J. Mech. Phys. Solids,* Vol. 18, 1970, pp. 115-126.

Lichinchi, M., Lenardi, C., Haupt, J., Vitali, R., "Simulation of Berkovich Nanoindentation Experiments on Thin Films using Finite Element Method," *Thin Solid Films,* Vol. 312, 1998, pp. 240-248.

Ma. D., Xu, K. and He, J., "Numerical Simulation for Determine the Mechanical Properties of Thin Metal Films using Depth-sensing Indentation Techniques, " *Thin Solid Films,* Vol. 323, 1998, pp. 183-187.

Marsh, D. M., "Plastic Flow in Glass," *Proc. R. Soc.* A279, 420(1964)

Merwin, J. E., and Johnson, K. L., "An Analysis of Plastic Deformation in Rolling Contact," *Proc. Inst. Mech. Eng.*, Vol. 177, 1963, pp. 676-690.

Hellgren, N., "Sputtered Carbon Nitride Thin Films," Ph.D. Thesis, Linkoping University, 1999

Oliver, W. C., and Pharr, G. M., "An Improved Technique for Determining Hardness and Elastic Modulus using Load and Displacement Sensing Indentation Experiments," *J. Mater. Res.*, Vol. 7, No. 6, June 1992, pp. 1564-1582.

Patel, J. J., "Investigation of the Scuffing Mechanism Under Starved Lubrication Conditions Using Macro, Meso, Micro, and Nano Analytical Techniques," M.S. Thesis, University of Illinois, May 2001.

Park, K. B., Ludema, K. C., "Evaluation of the plasticity index as a scuffing criterion" *Wear,* vol. 175, n. 1-2, Jun 1994, pp. 123-131.

Pethica, J. B., Hutchings, R. and Oliver, W. C., "Hardness Measurement at Penetration Depths as Small as 20 nm," *Phil. Mag. (A),* Vol. 48, 1983, pp. 593-611.

Pergande, S. R., “Use of Nano-indentation and Nano-scratch Techniques to Investigate Near Surface Material Properties Associated with Scuffing of Engineering Surfaces,” M.S. Thesis, University of Illinois, December 2001.

Rashid, M. and Seireg, A., “Heat Partition and Transient Temperature Distribution in Layered Concentrated Contacts. Part I and II,” *J. Tribology*, Vol. 109, 1987, pp. 487-495, pp. 496-502.

Schipper, D. J., “Transition in the Lubrication of Concentrated Contacts,” Ph.D. Thesis, University of Twente, 1988

Serpe, C. I., “The Role of Contact Compliance in the Deformation, Wear and Elastic Stability of Metallic Sliding Rings: Experiments and Computational Analysis,” Ph.D. Thesis, State University of New York at Buffalo, 1999.

Sheiretov, T. K., “Scuffing of Aluminum/Steel Contact Under Dry Sliding Conditions,” Ph.D. Thesis, University of Illinois at Urbana-Champaign, 1997.

Tabor, D., “Hardness of Metals”, 1951, Clarendon Press, Oxford

Wear Control Handbook, Peterson and Winer, Editors, Glossary of Terms and Definitions in the Field of Friction, Wear and Lubrication, pp. 1182.

Ye, N and Komvopoulos, K., “Thermo-mechanical FEM Analysis for the Head-disk Interface,” NSIC Presentation, 2001

Yoon, H. K., “Scuffing Under Starved Lubrication Conditions,” Ph.D. Thesis, University of Illinois at Urbana-Champaign, 1999.

Yu, Ning and Polycarpou, A.A., “Contact of Rough Surfaces with Asymmetric Distribution of Asperity Heights,” *ASME Journal of Tribology*, April, 2002, pp. 367-376.